Class. Quantum Grav. **25** (2008) 045002 (32pp) doi:10.1088/0264-9381/25/4/045002

A comparison of methods for gravitational wave burst searches from LIGO and Virgo

F Beauville[1], M-A Bizouard[2], L Blackburn[3], L Bosi[4], L Brocco[5], D A Brown[6,7], D Buskulic[1], F Cavalier[2], S Chatterji[6], N Christensen[8,9], A-C Clapson[2], S Fairhurst[7], D Grosjean[1], G Guidi[10], P Hello[2], S Heng[11], M Hewitson[11], E Katsavounidis[3], S Klimenko[12], M Knight[8], A Lazzarini[6], N Leroy[2], F Marion[1], J Markowitz[3], C Melachrinos[3], B Mours[1], F Ricci[5], A Viceré[10], I Yakushin[13] and M Zanolin[3]
(The joint LSC/Virgo working group)

[1] Laboratoire d'Annecy-le-Vieux de Physique des Particules, Chemin de Bellevue, BP 110, 74941 Annecy-le-Vieux Cedex, France
[2] Laboratoire de l'Accélérateur Linéaire, IN2P3/CNRS-Université de Paris XI, BP 34, 91898 Orsay Cedex, France
[3] LIGO—Massachusetts Institute of Technology, Cambridge, MA 02139, USA
[4] INFN Sezione di Perugia and/or Università di Perugia, Via A Pascoli, I-06123 Perugia, Italy
[5] INFN Sezione di Roma and/or Università 'La Sapienza', P le A Moro 2, I-00185 Roma, Italy
[6] LIGO—California Institute of Technology, Pasadena, CA 91125, USA
[7] University of Wisconsin–Milwaukee, Milwaukee, WI 53201, USA
[8] Carleton College, Northfield, MN 55057, USA
[9] European Gravitational Observatory (EGO), Via E Amaldi, I-56021 Cascina, Italy
[10] INFN Sezione Firenze/Urbino Via G Sansone 1, I-50019 Sesto Fiorentino; and/or Università di Firenze, Largo E Fermi 2, I-50125 Firenze and/or Università di Urbino, Via S Chiara 27, I-61029 Urbino, Italy
[11] University of Glasgow, Glasgow, G12 8QQ, UK
[12] University of Florida–Gainesville, FL 32611, USA
[13] LIGO Livingston Observatory, Livingston, LA 70754, USA

Received 20 June 2007, in final form 28 November 2007
Published 31 January 2008
Online at stacks.iop.org/CQG/25/045002

Abstract
The search procedure for burst gravitational waves has been studied using 24 h of simulated data in a network of three interferometers (Hanford 4 km, Livingston 4 km and Virgo 3 km are the example interferometers). Several methods to detect burst events developed in the LIGO Scientific Collaboration (LSC) and Virgo Collaboration have been studied and compared. We have performed coincidence analysis of the triggers obtained in the different interferometers with and without simulated signals added to the data. The benefits of having multiple interferometers of similar sensitivity are demonstrated by comparing the detection performance of the joint coincidence analysis with LSC and Virgo only burst searches. Adding Virgo to the LIGO detector network can increase by 50% the detection efficiency for this search. Another advantage of a joint LIGO–Virgo network is the ability to reconstruct the source sky position. The reconstruction accuracy depends on the timing

measurement accuracy of the events in each interferometer, and is displayed in this paper with a fixed source position example.

PACS numbers: 04.80.Nn, 07.05.Kf

(Some figures in this article are in colour only in the electronic version)

1. Introduction

The recent progress in the commissioning of gravitational wave interferometric detectors raises the possibility for performing joint data analysis between different collaborations. Indeed, the LIGO (two 4 km and one 2 km) [1] interferometers are at their design sensitivity, while the Virgo (3 km) interferometer's sensitivity is approaching its design expectations [2]. Moreover, efforts are currently being conducted in order to increase the duty cycle of each interferometer, and this will provide extended joint data-taking periods.

Gravitational wave (GW) burst events are characterized by their short duration (a few ms) and the absence of reliable theoretical predictions for their waveforms. The sources of GW burst events are numerous: massive star core collapse [3–6], the merging phase of coalescing compact binary systems forming a single black hole [7–10], black hole ring-down [11], astrophysical engines that generate gamma-ray burst [12] and even neutron star oscillation modes and instabilities. Newly born rapidly rotating neutron stars may emit GWs at the frequencies of the quasi-normal modes during the star's first minutes, and are expected to emit damped sinusoidal waveforms [13]. More exotic sources are possible, such as GW bursts emitted by cosmic strings [14]. Except for a few sources, the burst waveforms are poorly known and their amplitude is rather low. In this study, we did not consider well-modeled waveforms whose search is optimally done using matched filtering techniques. We concentrate on sources emitting poorly known waveforms.

It has been long acknowledged [17, 18] that GW burst detection can be enhanced by using information contained in a network of detectors spread around the world. Due to the time shortness of the burst GW and their weakness, we are obliged to work with quite high false alarm rates in each interferometer. With such a configuration, it is necessary to use a network of interferometers to reduce the false alarm rate (FAR). This is also the only way to disentangle a real GW burst event from transient noise events with sufficient confidence. Several methods and strategies can be used. There exist two categories of network data analysis: coincidence and coherent filtering. In the first approach, each interferometer data stream is analyzed, providing a list of event triggers. Triggers from the different interferometers are then compared to check if they are consistent with a real GW burst source. A coherent analysis uses all interferometer information by combining the input data streams or the filtered data streams into one single stream. The coincidence analysis is simpler to apply than the coherent analysis since it does not require the exchange of the detector data streams; this technique has been commonly used [19, 20]. On the other hand, the coherent analysis is expected to be, *a priori*, more powerful than the coincidence approach since a depreciated signal in a single interferometer can contribute to the global network output [18]. In this investigation, we focused on the coincidence analysis, trying to study all different aspects (including source location) since it is the simplest method to initially apply to multi-detector data. A similar comparison study for a coherent search is also underway for the LIGO–Virgo network.

The LSC burst search pipeline already performs coincidence analysis using LIGO's two well-aligned 4 km interferometers, and its 2 km interferometer. In addition, several joint searches with other detectors using real data have been done or are underway; an initial joint LIGO–TAMA coincidence search using real data has been reported in [21]. Joint searches for LIGO–GEO and LIGO–AURIGA [22] are underway. Similar efforts are carried out for binary inspiral GW searches. In the study presented in this paper, we analyze the potential benefits of a combined LIGO–Virgo detector network burst search; our study here is conducted using simulated data. This network is composed of three detectors of similar sensitivity. In actuality, having similar sensitivity plays a crucial role in the performance of a network (that is the reason why we did not consider the LIGO Hanford 2 km interferometer in this study. In addition, it could not be used to eliminate fake events due to environmental noise sources or detector artifacts since this study is carried out with the simulated data and not the real data). Nevertheless, while the LIGO detectors have the same orientation being separated by only 3000 km, the Virgo detector orientation and its distance with respect to the LIGO detectors imply that the Virgo and LIGO detectors do not have a maximal sensitivity simultaneously for the same region of the sky. Actually they are somewhat 'orthogonal'. It is then important to determine the gain of a coincidence search in such a network with respect to a search conducted using only the LIGO detectors. Note that a similar comparison study for the inspiral GW search has been carried out [23].

The paper is organized as follows. Section 2 contains a description of the characteristics of the data used for this analysis, including both the noise and source waveforms; these are the data that have been used for studying the different pipelines and the coincidence analysis. Section 3 summarizes the performance of seven different burst filters considered in this joint data analysis [24]. After having defined a benchmark, we evaluate and compare the intrinsic performance of each filter, and characterize each pipeline as is applied on both the LIGO and Virgo data streams. We address, at the end of this section, the issue of the burst signals' parameter space coverage by the different pipelines. We show, using simulated burst waveforms of different types, that the description of a burst GW with a few statistical parameters is not complete. We have investigated several strategies to carry out a coincidence analysis, taking into account that the three detectors do not have the same sensitivity with respect to the sky location for a particular source. The requirement for detecting a source in all the interferometers greatly decreases the FAR, but the detection efficiency may also drop drastically if the source is located in a region of the sky for which at least one detector has poor antenna response. We find that, for this particular network of detectors, requiring detection by any two of the three detectors gives an improved detection efficiency compared to the triple-coincidence detection at the same false alarm rate. Section 4 gives a summary of what can be achieved in such a network applying the different filters used by the two detector teams. We consider a source located at a fixed sky location (in the direction of the galactic center). We show the performance gain when adding a third interferometer of similar sensitivity but not well aligned with the first two. We have also estimated the gain of adding the event frequency information in the coincidence analysis. The benefits and disadvantages of a logical combination of filtered output obtained for each of the detector data streams (the so-called 'AND' and 'OR' analysis) have been investigated too and are summarized in section 5. Working with three interferometers spread over the world allows one to estimate the source sky location. In this study, we apply a method developed in Virgo [25] for estimating the source location. As an elementary building block of an all-time, all-sky search, we decided to look for a source that emits from a fixed location in the sky. The burst 'repeater' source was placed at the center of the Galaxy and the performance modulation due to the Earth's rotation has been studied with 24 h of simulated data. These results are given in section 6. Our results

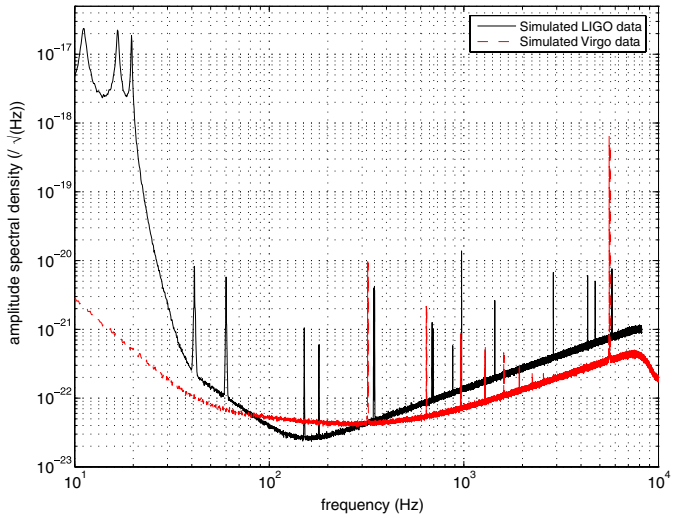

Figure 1. The LIGO (solid line) and Virgo (dashed line) simulated noise spectrum used in this study. The distortion close to the Nyquist frequency in the Virgo spectrum is due to the use of a low-pass filter applied before down-sampling the Virgo data generated at 40 kHz down to 20 kHz.

are summarized in section 7. Finally, one should note that, after a one year shutdown (for maintenance associated with further improving the detectors' sensitivity) starting in October 2007, the LIGO and Virgo detectors will be jointly operated as part of a single network.

2. Data set

2.1. Interferometer noise modeling

Simulated noise data streams have been generated for the LIGO Hanford (H1), LIGO Livingston (L1) and Virgo (V1) interferometers independently using the LSC [26] and Virgo [27] simulation tools. In both cases, a stationary and colored noise model has been used such as to reproduce the design sensitivity curve of the LIGO and Virgo interferometers as shown in figure 1. This includes thin thermal resonances (wire violin modes and mirror thermal noise) as foreseen in each detector; a Gaussian thermal noise modeling has been used for the Virgo noise generation, while a random phase modulation technique has been used for the LIGO noise simulation. The LIGO noise also includes lines due to electrical power supply (non-Gaussian process). In Virgo, the 50 Hz harmonics lines are subtracted in the main reconstructed gravitational wave strain applying a deterministic algorithm using an auxiliary channel which monitors the power supply of Virgo [28]. Two data sets have been produced. Initially, 3 h of H1 and V1 noise were created and used to characterize the burst filters and cross check the consistency of the different pipelines used in the LSC and Virgo. Then, 24 h of noise data have been produced for H1, L1 and V1 interferometers. These 24 h long data streams have been used for the coincidence analysis presented in this paper.

2.2. Signals

2.2.1. Waveforms and parameter space. Because many gravitational wave burst sources are currently not modeled in sufficient detail to allow matched filtering, most gravitational wave

Table 1. Boundaries of the parameter space for the burst signals studied. Time duration, peak frequency and bandwidth are the three parameters that have been chosen to describe the main features of expected burst signal waveform.

	Duration ($\Delta\tau$)	Peak frequency (ϕ)	Frequency bandwidth ($\Delta\phi$)
Minimum value	0.5 ms	50 Hz	5 Hz
Maximum value	50 ms	2000 Hz	1000 Hz

burst detection algorithms are designed to be insensitive to the details of the waveforms, and search through broad time and frequency ranges. However, in order to carry out a comparison of the different filters, we decided to use in this study three statistical variables as proposed in [29] to parametrize a burst signal. These three parameters are the time duration ($\Delta\tau$), the frequency bandwidth ($\Delta\phi$) and the peak frequency (ϕ) of the signal as defined using the first and second moments of the signal energy distribution in the time and frequency domains. Actually, the definition of the time duration and frequency bandwidth used in this paper differs from the one proposed in [29]: they are defined by the interval containing 50% of the signal energy, dropping 25% of the signal energy on both sides of the distribution. Note that $\Delta\phi$ and $\Delta\tau$ are constrained by some uncertainty relation [29, 30]:

$$\Delta\tau\Delta\phi > \frac{\Gamma}{4\pi}, \qquad \Gamma = 0.59\ldots. \tag{1}$$

This equation (also known as the Heisenberg–Gabor uncertainty relation) indicates that a signal cannot have arbitrarily small duration and bandwidth simultaneously.

The range values of those three quantities define a parameter space inside which the burst filters have to be as efficient as possible. The boundaries have been chosen taking into account theoretical predictions available in the literature and by the noise spectra shown in figure 1. They are given in table 1.

In order to fully characterize our burst filters, it is necessary to evaluate their performance using just a few waveforms that have different features and are well spread over the parameter space. We have used three different families of waveforms. First, the broadband Gaussian signals are of interest because many predicted core collapse simulation waveforms do have large peak structures corresponding to the bounce. Sine-Gaussian waveforms are narrowband signals that allow one to test a given frequency region. Finally, more complex waveforms predicted by the core collapse simulation, as described in [4], have been used; we have chosen two of them obtained with different assumptions on the model parameters. In both cases, the equation of state of the ideal gas is stiff, but in one case the differential rotation is small leading to type I (regular collapse) waveform (large negative peak followed by a ring-down phase). In the second case, the initial state is characterized by a rapidly rotating star with a large differential rotation producing a type II waveform characterized by multiple bounce collapse. The eight chosen waveforms, whose parameters are given in table 2, are represented in figure 2. Their frequency spectra are shown in figure 3.

The normalization of the signals can be done either by fixing the intrinsic signal strength ($h_{\rm rss}$) or by the intrinsic signal-to-noise ratio (SNR) of the signal seen in a detector. The latter quantity is more suitable if one wants to compare a filter's performance in interferometers with different sensitivity. On the other hand, in the case of a network analysis, it is mandatory to consider a source of a given intrinsic amplitude. This quantity is defined by

$$h_{\rm rss} = \sqrt{\int_{-\infty}^{\infty} |h(t)|^2 \, {\rm d}t}. \tag{2}$$

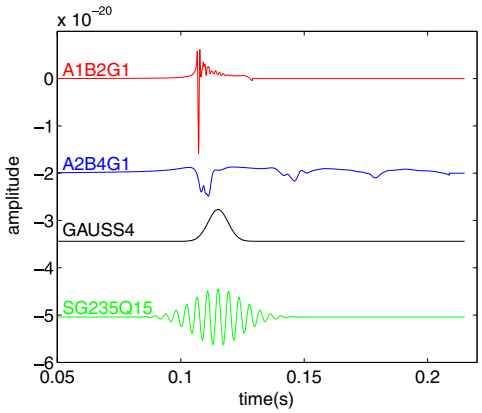

Figure 2. Waveform families of burst sources used in this study to estimate the performance of the different pipelines. DFM A1B2G1 and DFM A2B4G1: gravitational wave emitted during core collapse simulated by Dimmelmeier, Font and Mueller [4]. GAUSS4: Gaussian peak. SG235Q15: sine-Gaussian signal.

Table 2. Definition and parameter values of the eight waveforms used to estimate the burst filters' performance. For the DFM A1B2G1 and DFM A2B4G1 signals, the A, B and G parameters are defined in [4]. Information in the far-right column indicates whether the signal was used in the coincidence analysis described in section 4.

Name	Time domain formula	Parameter value	Coincidence
GAUSS1	$h(t) = \alpha \exp\left(\frac{-(t-t_0)^2}{2\sigma^2}\right)$	$\sigma = 1$ ms	Yes
GAUSS4		$\sigma = 4$ ms	Yes
SG235Q5	$h(t) = \alpha \exp\left(\frac{-2(t-t_0)^2\pi^2 f^2}{Q^2}\right)$	$f = 235$ Hz, $Q = 5$	No
SG235Q15	$\times \cos(2\pi f(t - t_0))$	$f = 235$ Hz, $Q = 15$	Yes
SG820Q5		$f = 820$ Hz, $Q = 5$	No
SG820Q15		$f = 820$ Hz, $Q = 15$	Yes
DFM A1B2G1		$A = 1, B = 2, G = 1$	Yes
DFM A2B4G1		$A = 2, B = 4, G = 1$	Yes

The intrinsic SNR seen in a detector is given by the SNR of a matched filter

$$\rho = 2\sqrt{\int_0^\infty \frac{|h(f)|^2}{S_h(f)}\,\mathrm{d}f}, \tag{3}$$

where $S_h(f)$ is the one-sided power spectrum of the detector noise.

For the estimation of the pipelines' performance given in section 3, we have considered that the detectors are optimally oriented with respect to the source (no antenna patterns have been considered).

The free parameters of the different pipelines studied here have been chosen such as to maximize the detection efficiency of the eight chosen waveforms. In section 3.4, we address the issue of a possible dependence of the pipeline parameters' tuning upon the waveforms considered. For that purpose, we have extended the set of waveforms, and studied a larger set of core collapse simulated waveforms (50). We have also added 50 waveforms which fill the region of the parameter space outside the 'minimal uncertainty' region. They are generated using band-passed white noise.

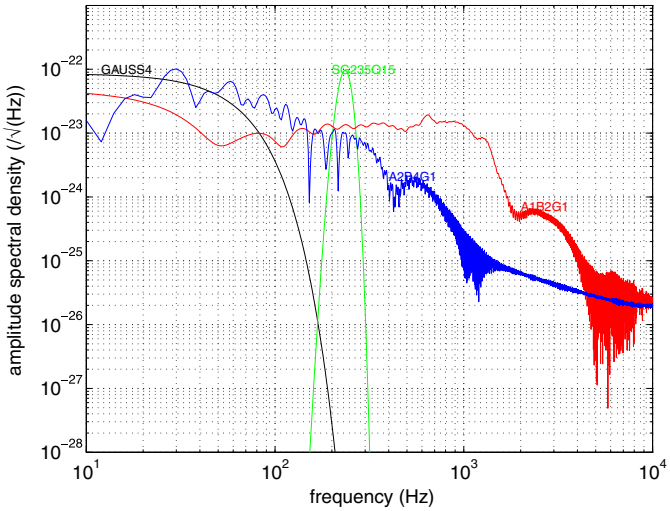

Figure 3. Spectrum of the waveform families of burst sources used in this study to estimate the performance of the different pipelines. DFM A1B2G1 and DFM A2B4G1: gravitational wave emitted during core collapse simulated by Dimmelmeier, Font and Mueller [4]. SG235Q15: sine-Gaussian signal. GAUSS4: Gaussian peak. All waveforms have been normalized such that $h_{\rm rss} = 3.59 \times 10^{-22}\sqrt{\rm Hz}$. This value corresponds to a SN source located at 10 kpc emitting a A1B2G1 waveform.

2.2.2. Coincidence analysis injections. For the coincidence analysis described in sections 4–6, we located the source in the direction of the galactic center. The waveforms are linearly polarized, with the polarization angle uniformly distributed. In addition to the unknown polarization angle, the response of the detector to a GW depends on the sky position of the source. A source of constant intrinsic emission strength located in the direction of the galactic center would emit signals whose amplitude measured by a detector would then vary over 24 h as shown in figure 4. We have used 24 h of simulated data in order to study, on average, the effect of the Earth's rotation on the detection performance. Due to the use of non-astrophysical waveforms (with the exception of supernova core collapse), we cannot use the distance to fix the strength of the signal. We have then normalized the six waveforms such that over 24 h there is only one injected event seen with a SNR of 10 or greater in all the three detectors. For the supernova core collapse, this scaling corresponds to a distance of 4.8 kpc for DFM A1B2G1 and 3.6 kpc for DFM A2B4G1.

3. Burst search methods and their performance

In this investigation, we have studied different burst detection algorithms. We compared their performance in order to determine if they cover the variety of possible astrophysical waveforms. Indeed, before performing a network analysis with some of them it is important to know how they behave individually. For each filter, we measure its detection efficiency as a function of the false alarm rate. Then, the arrival time of the signal in each interferometer has to be determined with very good accuracy (of the order of 1 ms) in order to be able to reconstruct the position of the source in the sky. In the following, we briefly describe the different pipelines used in this study. It is important to note that some of these filters require whitened data. This pre-processing stage is performed both for the LSC and Virgo pipelines

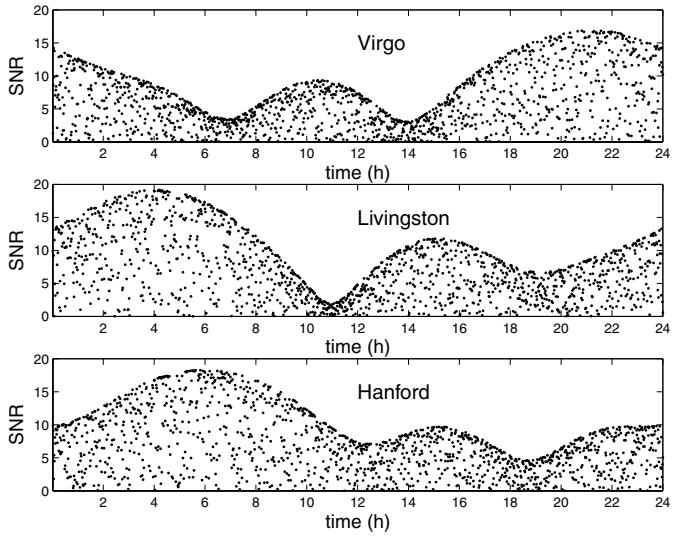

Figure 4. Signal-to-noise ratios of DFM A1B2G1 signals emitted by a source located in the direction of the galactic center over 24 h. The SNRs were computed for the H1, L1 and V1 detectors, taking into account their antenna pattern at the signal arrival time (note the envelope of the distributions). In this study, the source is polarized with the polarization angle uniformly distributed; this produces the distribution of values inside the envelope.

using a linear predictive error filter. These have been developed in each collaboration, see for instance [31, 33].

3.1. Pipeline description

We utilized search methods operating in the time and time–frequency domains. In addition, correlator filters were also applied. Two of these pipelines (KW and QT) have been developed in the LSC, while the others have been developed in the Virgo.

3.1.1. Excess power methods.

- *Power filter (PF).* PF [32] searches on whitened data for a power excess using different time analysis windows and different frequency bands chosen such that the product of the frequency width and the time duration remains constant. In order to cover the parameter space, five time windows have been chosen: 64, 128, 256, 512 and 1024 bins for the LIGO and Virgo data; the bin size is defined as the sampling time for the data, which is $1/16\,384$ s for LIGO and $1/20000$ s for Virgo. The windows duration is hence a little different for the two data sets because of the different data sampling rates. The PF has been tuned, in this study, to cover all frequencies between 40 Hz and 2000 Hz. In the time–frequency plane, the PF statistics are derived by taking the logarithm of the spectrogram.
- *Kleine Welle (KW).* KW searches for excess signal energy in the dyadic wavelet decomposition of a whitened time series. The wavelet transformation is evaluated at distinct scales (which is directly related to frequency) and involves stretching and contracting a mother wavelet (in this case the *Haar* wavelet) by the scale factor before using it to filter the time series [33]. In this study, the frequency range covered by KW

was from 64 Hz to 1064 Hz for the H1 and L1 data, and from 78 Hz up to 1250 Hz for the V1 data. As the input time series is whitened by the use of a linear predictive filter prior to the wavelet decomposition, the wavelet coefficients calculated at each scale follow a Gaussian distribution and are normalized to unity variance. KW identifies events in the time series by clustering large-amplitude coefficients which are nearby in time and scale.

3.1.2. Time domain filters.

- *Mean filter (MF).* MF searches for an excess in a moving average computed on the whitened data. Ten different analysis windows, with durations varying from 0.5 ms up to 10 ms, are used. The moving stride of each window is 1 bin. It has been shown that the analysis window size has to be matched with the duration of the signal to have the best detection result [18]. Note that the MF behaves like a low-pass filter and, given the choice of the windows' size, the MF could not explore the frequency domain beyond 1 kHz. A threshold is applied on each analysis window output, producing triggers which may overlap. They are then clustered if they coincide within a time window equal to 12 times the size of the analysis window. This value corresponds to the optimal signal efficiency for the chosen threshold (SNR $>$ 4) obtained on simulated Gaussian data in which signals, such as the ones used in this study, have been injected. Finally, note that no information about signal frequency is provided.
- *Alternative linear filter (ALF).* The ALF aims at detecting large slopes associated with peaks in the data in ten moving analysis windows whose duration varies between 0.5 ms and 15 ms. The moving stride of each window is 1 bin. The frequency range that ALF can explore is below 1 kHz. A straight line is fit to the data in an analysis window. The two non-independent fit results, namely the line slope and the offset value, are then combined quadratically to define the ALF statistics. Concerning the optimal analysis window size to detect a peak, it has been shown that the window size has to be 30% larger than the duration of the peak. This effect is due to the noise standard deviation which is reduced if the computation is done over a larger window [34]. The pipeline of ALF is identical to that of the MF filter concerning the events clusterization.

3.1.3. Correlator filters.

- *Peak correlator (PC).* This is a matched filter using the Gaussian waveform templates [15]. The Gaussian templates have been chosen such that the minimum match is better than 99% for the Gaussian peaks whose σ is between 0.2 ms and 6 ms (eight templates). That corresponds to a maximum frequency of about 900 Hz. Note that the PC has been implemented using the Welch overlapping scheme [35] which optimizes the computing cost in the case of small template size. The events obtained after thresholding are then clustered using only time coincidence information.
- *Exponential Gaussian correlator (EGC).* The complex exponential Gaussian correlator produces a time–frequency representation of the data by applying the correlation relation for a list of templates of the same family,

$$\Phi_{f_0,Q_0}(t) = \mathrm{e}^{-2(\pi f_0/Q_0)^2 t^2}\, \mathrm{e}^{\mathrm{i}2\pi f_0 t}, \tag{4}$$

with f_0 and Q_0 being the central frequency and the quality factor of the template, respectively.

Template selection relies on a tiling algorithm valid for any two-parameter matched filter bank [36]. Two tiling zones have been defined in order to optimize the visibility of non-oscillatory waveforms, while covering a large range of periodic signals with a reduced

number of templates (122). The first zone covers $10 \leqslant f \leqslant 1000$ Hz and $1 \leqslant Q_0 \leqslant 3$, while the second spans $150 \leqslant f \leqslant 1000$ Hz and $1 \leqslant Q_0 \leqslant 17$. The event duration covered is from 0.2 ms to 50 ms. Because the frequency coverage is redundant, templates are grouped in frequency bands 50 Hz wide, where they are ordered by decreasing quality factor. Events are then identified as local energy excesses. More details can be found in [37].

- *Q-transform (QT).* QT is a multi-resolution search for statistically significant signal energy in the time–frequency plane [33]. It is equivalent to a matched filter search for sinusoidal Gaussian bursts with unknown phase in the whitened data stream. The data are first whitened by the linear predictive filtering. The resulting whitened data are then projected onto an over-complete basis of the Gaussian-windowed complex exponentials within a targeted range of frequency and Q (the ratio of frequency to bandwidth). For this study, the Q-transform was tuned to search the frequency range from 64 Hz to 1024 Hz and the Q-range from 3.3 to 22 corresponding to an event duration range from 0.5 ms up to 50 ms. Candidate events are then described by the most significant set of non-overlapping time–frequency tiles that exceed a specified significance threshold.

Note that while the QT and EGC filters look similar, they are actually implemented differently. The noise normalization is done externally for QT, while EGC performs matched filtering. The event extraction is different; EGC includes all neighboring templates, while QT prunes overlapping templates.

3.2. Event trigger definition

Each of the burst search filters applies a threshold on the filter output. The filter output is either defined as an energy in a time–frequency grid or as a SNR in the time domain. This is performed for several values of the parameters (frequency band, window size, template). For time–frequency methods, all nearby pixels are clustered and the energy of the cluster is defined as the sum of the energy of the pixels according to a well-defined prescription developed in each of the methods. After thresholding, we obtain a collection of events defined by a start time, an end time, a peak time and the corresponding maximum filter output. In addition, filters designed for providing localization in the frequency domain (QT, KW and EGC) yield an estimation of the event bandwidth and the peak frequency, corresponding to the frequency of the template with the highest SNR.

Almost all the burst filters deal with several analysis windows, templates or time–frequency planes. In the case of a signal, several nearby templates or time–frequency planes are expected to trigger, corresponding (in actuality) to the same event. All burst pipelines thus apply an event clustering algorithm that gathers all primary defined events corresponding to the same signal event. The clustering algorithm usually depends on the filter type: time–frequency, correlators and time domain filters.

3.3. Detection performance

One way to quantify the detection potential of a burst search filter is through the determination of receiver operator characteristic (ROC) curves for each filter and for each family of waveforms. The ROC curve shows the filter detection efficiency versus the false alarm rate (FAR). The FAR is usually a free parameter which is fixed differently with each interferometer data set according to the type of analysis; a discovery search requires one to have very few false alarms in order to select golden events which are then studied deeply in detail (waveform, frequency content, arrival time consistency), while to better understand the

Table 3. Necessary ρ for 50% efficiency at FAR = 0.01 Hz for H1 (up) and V1 (bottom) data. The symbol '–' means that the performance was too poor to be estimated.

	PF	KW	QT	PC	EGC	MF	ALF
H1							
A1B2G1	6.7	7.5	6.5	5.1	5.1	7.3	6.7
A2B4G1	7.4	7.7	6.4	5.8	6.9	7.0	6.6
GAUSS1	6.2	7.0	5.5	4.9	5.6	6.7	6.1
GAUSS4	7.2	8.0	5.6	4.9	5.9	7.7	6.4
SG235Q5	7.7	6.9	5.1	6.1	5.8	7.5	7.0
SG235Q15	10.5	8.6	5.1	–	6.0	10.6	9.9
SG820Q5	5.9	7.4	5.2	–	6.0	8.2	6.9
SG820Q15	5.6	9.1	5.1	–	5.8	11.6	9.7
V1							
A1B2G1	5.9	7.1	6.6	5.6	5.3	6.1	6.0
A2B4G1	6.6	7.5	6.8	5.8	6.5	6.3	6.0
GAUSS1	5.9	6.5	5.9	4.9	5.5	6.0	5.7
GAUSS4	7.3	8.4	7.0	5.2	5.7	6.2	5.6
SG235Q5	6.6	6.9	5.2	6.6	5.5	7.5	6.9
SG235Q15	8.9	8.8	5.1	–	5.7	11.7	9.8
SG820Q5	5.7	7.5	5.1	–	5.7	8.6	7.1
SG820Q15	5.7	9.3	5.3	–	5.6	15.9	10.2

statistical properties of the background noise (gaussianity, stationarity) it is necessary to have a large FAR. Moreover, in a network analysis with non-correlated noise in the interferometers, a simple coincidence analysis reduces the final FAR by a few orders of magnitude with respect to the single-interferometer FAR (which can be chosen rather high). This is demonstrated in section 4. The ROC curves for the eight test-case waveforms have been computed for all burst filters and for different values of the strength of the signal. In particular, we checked the consistency of the results obtained with the H1 and V1 data. In the following, we summarize the main results about the ROC curves estimated for a FAR varying from 10^{-4} Hz (one false alarm per 3 h) to 10^{-1} Hz (a single-interferometer FAR which can be easily handled in a network coincidence analysis). Figure 5 shows the ROC curves (using the H1 data) for four of the eight waveforms: A1B2G1, SG235Q5, GAUSS1 and SG820Q15. They have been obtained for a signal injected with an intrinsic SNR of 7 (see equation (3)). This SNR value emphasizes the performance differences; with a higher value, for many pipelines the efficiency saturates at 100% over the full FAR range. Table 3 gives the values of a signals' intrinsic SNR necessary to have a detection efficiency of 50% at a fixed FAR of 0.01 Hz. These values have been obtained by fitting the curve of efficiency versus the signal h_{rss} with an asymmetric sigmoid function, as defined in [20].

The first comment about these numbers is that filters perform differently according to the waveforms. There is no one filter that performs better than all of the others when considering such a variety of waveforms. One can also note that the largest performance spread corresponds to sine-Gaussian signals, as shown in figure 5. The QT and EGC have rather constant and good performance for all the tested waveforms, and as expected perform very well for all sine-Gaussian waveforms. One can, however, remark that QT performs slightly better than EGC on the test-case sine-Gaussian signals, especially for the H1 data. This is partly due to the fact that QT is using an over-complete template bank, and also due to different event extraction for QT and EGC. Moreover, one should note that EGC explores the low-frequency region more effectively than QT (the lowest frequency of EGC is 10 Hz, while QT starts at

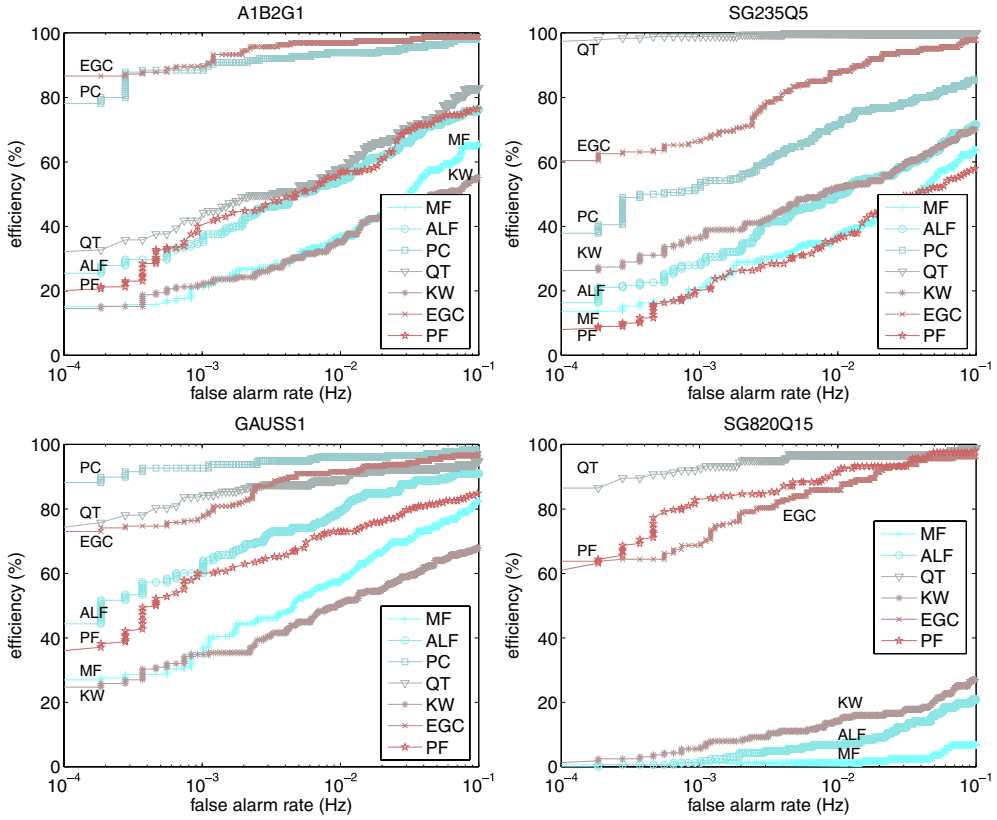

Figure 5. ROC curves obtained from the bank of filters studied using four different waveforms (DFM A1B2G1, SG235Q5, GAUSS1 and SG820Q15). The signal waveforms have been injected into H1 noise with an intrinsic SNR of 7.

64 Hz). That explains why EGC obtains a better performance on Gaussian signals for the V1 data.

The relative low efficiency of KW with respect, for instance, to the QT pipeline is partly due to the fact that QT is using an over-complete template bank, and to the fact that the Haar function basis does not optimally span the region at high Q. Moreover, KW has a totally orthogonal basis. The test-case signal's SNR is most likely spread over several wavelet functions. The KW clustering algorithm tries to recover as much signal as possible, but cannot be as efficient as an optimal matched filter (as extra noise is introduced).

The other filters have less consistent results. This is especially true for the case of MF, ALF and PC. For instance MF, which averages the data for a given duration, has a poor (expected and observed) performance on sine-Gaussian signals. For Q constant, MF's performance decreases as the frequency increases; at a fixed frequency, MF's performance decreases as Q increases because the number of cycles increases. An equivalent argument explains the poor performance of ALF and PC for sine-Gaussian waveforms. If the intrinsic strength of the signal is spread over many cycles, ALF is strongly disabled whatever the size of the analysis window. Conversely, PC and ALF perform well for signals whose waveform is peak-like (the DFM and Gaussian waveforms). PC is, *a priori*, an optimal filter for Gaussian peaks. PF's performance is rather constant; it obtains intermediate performance on the DFM and Gaussian

signals. For sine-Gaussian signals, PF is usually very competitive but, as can be seen in figure 5, this is not the case for the SG235Q5 signal. This loss of efficiency is due to the choice, done *a priori*, of the frequency windows in which the power is calculated. The frequency region around 235 Hz is split over two windows.

It is also interesting to note some differences in the results obtained with the H1 and V1 data for signals having the same SNR, as reported in table 3. The difference never exceeds a maximum of 25%, and is different from one pipeline to another; QT and PC perform better with the H1 data, while the other pipelines perform slightly better on the V1 data. The difference depends also on the waveforms; the largest difference is found for the GAUSS4 signal. The bad performance of QT on the GAUSS4 signal for V1 compared to H1 data is due to the fact that the amplitude of the GAUSS4 signal is lower in V1 than in H1 data. Indeed, this signal has its main frequency content at very low frequency (below 100 Hz as shown in figure 3). The waveforms are normalized for V1 and H1 such that their SNR is constant in both detectors. Since the Virgo PSD is lower at low frequency than LIGO's PSD, the overall amplitude of the GAUSS4 waveform is lower for V1 compared to H1. But, since the QT low-frequency cutoff (64 Hz) is the same for V1 and H1, QT will recover a smaller fraction of SNR of this signal in V1 compared to H1.

3.4. Waveform robustness results

In this study, the parameters of the algorithms have been chosen in order to cover a large fraction of the parameter space defined in section 2.2.1. However, many of the pipelines actually use parameters which have been tuned for real data analysis in the LSC or Virgo burst searches. The performance of the pipelines, described above, have been estimated using eight waveforms spread over the parameter space. In order to test the robustness of the pipelines' performance to a wider set of burst waveforms spread over the signal's parameter space, we have computed the efficiencies for all pipelines at a given FAR using 100 waveforms chosen randomly as follows:

- Fifty waveforms produced by core collapse simulations (SN) extracted from [3–5].
- Fifty band-passed white noise (WN) signals: white noise is filtered in frequency and then a Gaussian window is applied in the time domain in order to limit the duration of the signal.

The band-passed white noise signals have been considered in this study in order to easily span the parameter space, especially in the region of high-frequency and large-frequency bandwidth. The parameters of the waveforms are given in the appendix. Figure 6 shows the pipelines' efficiency obtained for a FAR of 0.001 Hz with the V1 data, represented in the two-dimensional plane defined by the central frequency and the time–frequency volume (the product of the duration with the frequency bandwidth). An important point concerns the location of the different families of waveforms; although the three parameters, based on the moments of the distribution of the signal energy in the time and frequency domains, obey the uncertainty relation (see equation (1)) that explain the borders of the plots, the different signal families do not populate exactly the same region of the parameter space. The core collapse signals (SN) are all concentrated in a region for which the central frequency is lower than 700 Hz, while the frequency bandwidth can be as large as 600 Hz, and the time duration is well spread over the full range. The band-passed WN signals cover the full parameter space, as defined in section 2.2.1. Note that the very low bandwidth WN signals look like sine-Gaussian signals (a Gaussian window is applied in the time domain on all filtered white noise waveforms in order to limit the duration).

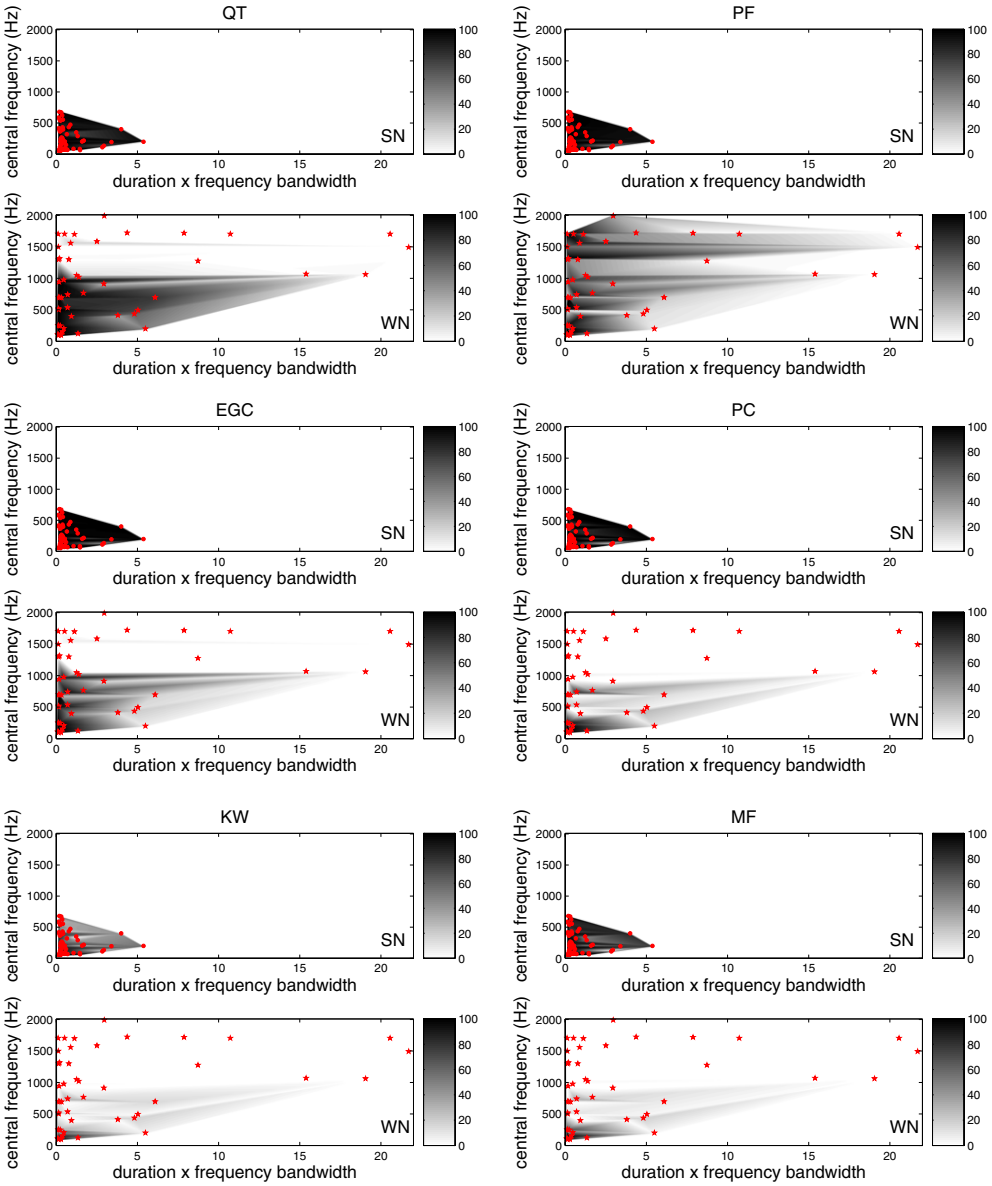

Figure 6. Pipeline efficiencies obtained for two families of waveforms: SN (top) and WN (bottom). The efficiency of six pipelines (ALF pipeline is not represented here, but is very similar to MF) is shown in the two-dimensional plane of the central frequency versus the time–frequency volume. The efficiency has been computed using the Virgo noise data for a FAR of 0.001 Hz and a signal SNR of 10.

One can note that the overall parameter space coverage performances obtained by the different pipelines are not identical. PF is the only pipeline which has been configured, in this analysis, to include data in the 1–2 kHz range in its analysis. Naturally, a pipeline that has been tuned to cover the full parameter space has a higher FAR at a given efficiency. This can be translated into an efficiency drop of a few percent for a given FAR for all signals.

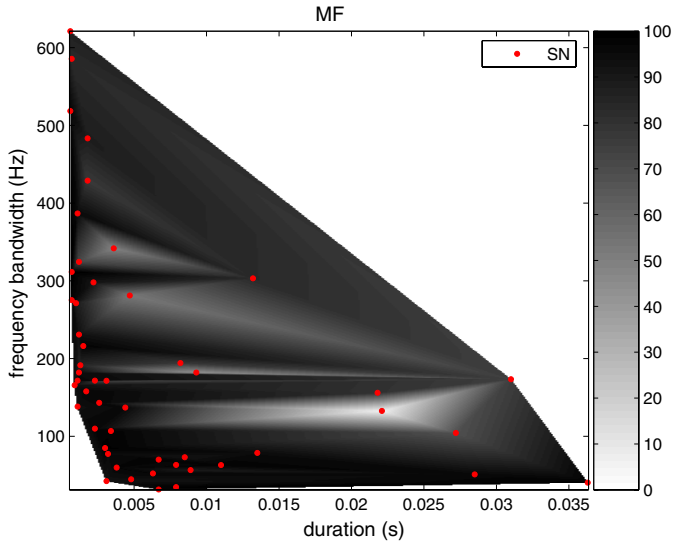

Figure 7. MF pipeline efficiencies obtained for 50 SN waveforms as a function of the duration and bandwidth of the signal. The efficiency has been computed for a FAR of 0.001 Hz and the signal SNR is 10.

The performance of the other detection pipelines drops above 1 kHz. It should be mentioned that for MF, ALF and PC the tuning is intrinsically limited; the only free parameter of these pipelines is the time duration of the signal, thereby limiting the frequency domain exploration. KW is the filter for which the performance gets worse as the time–frequency volume increases. Actually, as already mentioned in section 3.3, because of the choice of the Haar function basis the KW performance drops for long-duration signals. One can also note that all pipeline performances are maximum in the region of low or moderate time–frequency volume where the actual SN signals are located. All the pipelines obtain their best performance on the SN signals and fail mostly at detecting the WN signals. Concerning the very low bandwidth signals which look like sine-Gaussians, QT performs very well as expected, while the EGC efficiency is not as good for sine-Gaussian signals with very low-frequency bandwidth. EGC is expected to be an optimal filter for sine-Gaussian, as is QT. The loss of efficiency is due to the choice of template placement for EGC, which is non-optimal in the region of the parameter space populated by those particular sine-Gaussian signals.

Focusing on the SN family, one can see that all pipeline performances drop for a particular SN signal, although they all maintain a very high efficiency for the others. For instance, the MF efficiency decreases to 6% for this one SN signal, while it remains always above 75% for the 49 other SN signals, and even better for similar signals in the parameter space neighborhood, as shown in figure 7. This efficiency drop is primarily explained by the peculiarity of the shape of this core collapse simulated signal, which does not show any peak usually associated with core bounce but rather rapid oscillations. This particular signal corresponds to a rapid collapse for which the first peak usually present in the SN signals is strongly suppressed (non-rotating model). The waveform of this SN signal is shown in figure 8. This example suggests that the three parameters used to describe a gravitational burst event are not complete. This fact is even clearer when one considers the WN signal results; in the region of the SN signals, the overall performance of all pipelines on WN is lower than for SN signals. Moreover, for

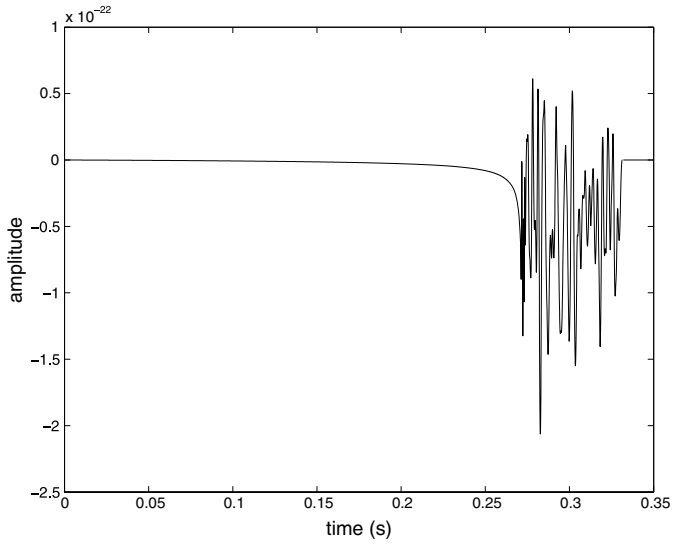

Figure 8. The waveform of the simulated SN signal (extracted from [5] and labeled as s15nonrot in the appendix) for which the efficiency of all pipelines is low compared to other SN signals close to it in the parameters space defined in this study.

all pipelines, there is a region, inside the SN area (for central frequency between 400 Hz and 500 Hz), where the efficiency drops to a very low value for WN signals, while there are some SN events with identical parameters for which the efficiency is close to 100%. This indicates again that the various pipelines are taking into account some signal shape information that might be badly modeled with the three parameters used for this study. But this present study is limited by the number of waveforms tested.

3.5. Timing accuracy

It is crucial to accurately estimate the arrival time of a signal in each gravitational wave detector in order to perform an interferometer network coincidence analysis, reconstruct the source sky location, and to perform a coincidence analysis with other messengers (neutrinos, gamma-ray bursts, etc). It is especially important to prove that we are able to determine the arrival time of a signal in each of the interferometers with an accuracy that is much better than the time of flight of a signal between two interferometers (10 ms between the LIGO interferometers, and 27 ms between the Virgo and LIGO interferometers). For the bank of burst filters investigated, we have studied the statistical properties of the signal arrival time estimators that can be built for each of the filters. The most natural and convenient definition of the signal arrival time is the time for which the amplitude is maximum. Taking this definition, an estimator for determining the signal arrival time has been defined based upon the filter statistics. Those estimators can be biased and/or can have different intrinsic accuracy depending on the waveform of the signal. We report in table 4 the bias and the standard deviation of the distribution of the difference between the true arrival time and the estimated arrival time obtained for each waveform injected each 60 s in the V1 3 h data stream. The signal strength was SNR $= 10$ and the detection efficiency was fixed by a common FAR of 0.1 Hz for all waveforms.

Table 4. Standard deviation and bias of the signal arrival time (in ms) obtained by estimators built from the burst filters. The values have been obtained for the different test-case waveforms selected at a false alarm rate of 0.1 Hz for the V1 data. The signal SNR is 10. When the efficiency is low, it has not been possible to estimate all the quantities for the PC filter estimator.

	PF	KW	QT	PC	EGC	MF	ALF
Standard deviation							
A1B2G1	0.05	0.5	0.2	0.04	0.03	0.05	0.3
A2B4G1	0.7	2.6	1.4	0.2	0.4	0.5	2.2
GAUSS1	1.2	1.4	0.8	0.1	0.2	0.8	1.5
GAUSS4	2.7	4.3	2.3	0.3	0.7	0.6	3.2
SG235Q5	1.4	0.9	0.9	1.2	0.5	1.3	1.1
SG235Q15	4.8	3.3	2.5	–	1.6	4.4	4.1
SG820Q5	0.2	0.3	0.2	–	0.2	0.3	0.3
SG820Q15	0.6	1.1	0.7	–	0.5	1.3	1.1
Bias							
A1B2G1	0.2	0.3	−0.1	−0.05	−0.06	0.03	0.1
A2B4G1	1.9	4.9	−1.7	−1.3	−1.4	2.1	0.7
GAUSS1	1.7	3.4	−0.05	−0.01	0.01	2.3	1.7
GAUSS4	4.1	10.7	−0.4	−0.03	−0.03	3.4	6.4
SG235Q5	0.6	1.3	−0.07	0.02	0.02	0.7	0.7
SG235Q15	1.1	0.8	0.06	–	0.1	0.2	0.6
SG820Q5	0.2	0.2	−0.01	–	0.01	0.1	0.1
SG820Q15	0.2	0.3	−0.04	–	0.03	0.3	0.2

As expected, the estimator built with the peak correlator filter output (PC) has a very good accuracy (less than 0.3 ms) and almost no bias for all signals which concentrate their energy in one peak (the Gaussian and DFM A1B2G1 signals). The best accuracy is obtained on the DFM A1B2G1 signal for all estimators. This is due to the small width of the DFM A1B2G1 peak (a width of 0.25 ms, compared with the 2.35 ms width of GAUSS1). Nevertheless, it has not been possible to characterize the arrival time estimator of PC on sine-Gaussian signals due to its very low efficiency. For the DFM A2B4G1 waveform, the bias and standard deviation of all estimators are rather large compared to other DFM waveforms due to the presence in the waveform of three peaks of decreasing amplitude separated by 5 ms. The energy of DFM A2B4G1 is more spread out in the time–frequency plane, decreasing the localization ability for all filters. For sine-Gaussian waveforms, the QT, EGC and PF estimators obtain the best time accuracy; they are the most efficient filters for detecting these signals. It is obvious that there is a direct relation between a low-efficiency filter and poor time accuracy estimator (see, for instance, PC or MF on sine-Gaussian waveforms), but an efficient filter does not necessarily allow one to build a good estimator of the arrival time (see, for example, ALF on Gaussian peak waveforms).

The large bias (up to 6.4 ms for ALF) of the time domain filters, KW and PF estimators, is explained partly by the whitening process applied to the data. Indeed, as shown in figure 9 for V1, the whitening filter strongly distorts a Gaussian waveform. The whitening can transform a Gaussian peak into a bipolar waveform due to the spectral power shape. As a consequence, the filter triggers on one peak or another depending on noise fluctuations. The whitening distortion effect is important for the signals that have a large SNR content at low frequency, such as the Gaussian signals. The distortion is even stronger in the case of H1 noise since the power spectrum is higher in the low-frequency region (the effect of the whitening process is then larger in this region). For instance, the MF estimator bias for a 4 ms Gaussian peak

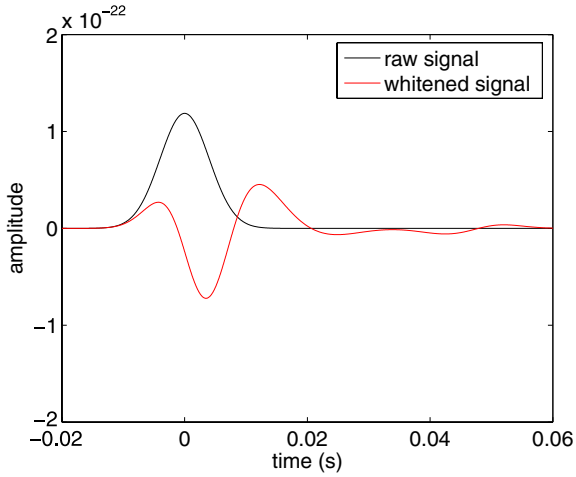

Figure 9. The effect of the V1 whitening pre-processing filter applied on a Gaussian pulse of 4 ms width (GAUSS4).

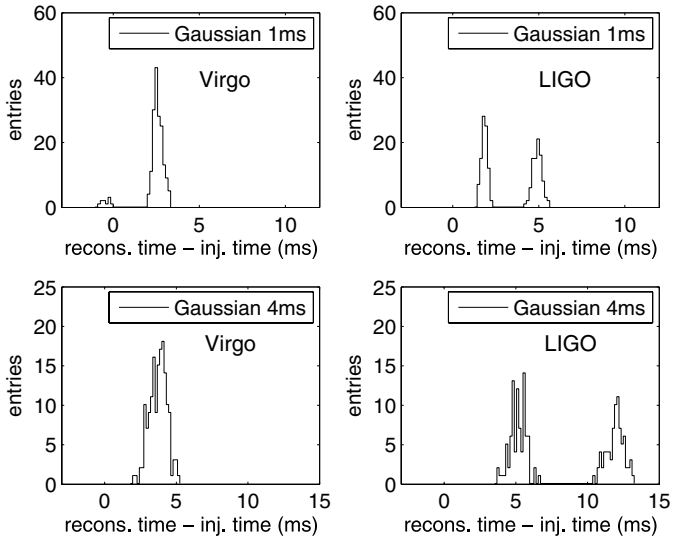

Figure 10. Distributions of the difference between the reconstructed arrival time of a Gaussian signal (the width of 1 ms and 4 ms) and the injected value. These distributions were created using the MF timing estimator on the V1 and H1 data.

increases from 3.4 ms to 8.3 ms and its standard deviation from 0.9 ms to 3.4 ms, as shown in figure 10. Moreover, the whitening algorithm used by the PF, MF and ALF pipelines was not a nonzero phase filter. It thus introduces an additional time delay that adds to the bias due to waveform distortion. This delay depends on the power spectrum and the waveform. Finally, it is important to note that for many waveforms the arrival time estimation accuracy for a signal of intrinsic SNR of 10 can be as good as 1 ms. The standard deviation of the arrival time estimation scales roughly inversely with the signal SNR [38].

4. Coincidence analysis

4.1. Description

As shown in section 3, the FAR of the burst signal filters will remain quite high if we do not want to miss the rare astrophysical event. For example, a DFM A1B2G1 signal of $\rho = 6$ can be observed with a detection efficiency between 30% and 75%, but with a 0.01 Hz FAR leading to 864 false alarm events per day. Furthermore, the FAR for burst searches on real data tend to be much higher than those on Gaussian stationary data. One way to significantly reduce the FAR while keeping the detection efficiency above, say 50%, is to request that the arrival times of signals in the detectors be compatible with the travel time of the wave between interferometer locations. This assumes, of course, that detector noise fluctuations are not correlated. It also requires the timing error to be less than the travel time of the wave which is the case for all pipelines (except maybe KW for Hanford–Livingston coincidence, see table 4). In the case of a source of unknown position, the signal arrival time difference must be less than the maximum travel time Δ_{12} between two detectors. If the source position is known (for example, a detected optical counterpart) one can use the exact travel time of the signal between the detectors. However, this constraint does not provide a large false alarm reduction.

In this study, the source has been located in the direction of the galactic center, while we are performing an all-sky blind search using only the timing information (the use of the frequency characteristics has been studied separately). Assuming that the trigger time distribution follows a Poisson distribution, the FAR of a coincidence analysis, performed with two interferometers' output, is given by the product, $fa_1 \cdot fa_2 \cdot 2\Delta_{12}$, where fa_i are the FARs in the detector pipelines and Δ_{12} is the maximum travel time of a signal from one detector to the other. If we consider a single experiment FAR of 0.1 Hz, the double experiment coincidence analysis FAR is around 0.2 mHz (for $\Delta_{12} = 10$ ms). However, if a detector in the network is not well aligned with respect to the others, the signal may be not visible in at least one detector, even with a high single interferometer FAR. It is thus important in the given network (the Hanford, Livingston and Virgo observatories) to study how the different network configurations compare. Hence we consider coincidence between these three interferometers (three-fold coincidence), and coincidence between two detectors among the three (two-fold coincidence). We also consider the combination of the two-fold coincidences in order to cope with the misalignment of the LIGO–Virgo detector network.

4.2. Two-fold and three-fold analysis

The seven pipelines have been applied on the three data streams in which six different waveforms were injected each minute (the maximum rate to avoid any bias of the pipeline output estimation due to the presence of too many signals in the data segment). The source of given h_{rss} is located in the direction of the galactic center and its polarization angle is varied randomly as explained in section 2.2.2. We produced event lists corresponding to a rate of false alarm events of 0.1 Hz. The efficiencies obtained by the pipelines for the six waveforms are reported in table 5.

4.2.1. Coincidence analysis. Starting from the generated list of events (FAR is 0.1 Hz), each pipeline looked for two-fold and three-fold coincidences. The coincidence time windows applied for a blind search take into account the maximum light travel time between pairs of interferometers and the maximum timing accuracy (bias and standard deviation) obtained for the test-case waveforms given in table 4. Using the results presented in table 4, we

Table 5. Detection efficiencies (in percent) obtained by the seven pipelines for a source located in the galactic center for a FAR of 0.1 Hz. The efficiencies have been estimated for each detector data stream: Hanford (H1), Livingston (L1) and Virgo (V1). In this study, the source emits signals regularly over 24 h (one emission each minute with the random polarization angle as explained in section 2.2.2); we tested six different waveforms. The pipelines' efficiencies thus take into account the modulation of the signal strength due to the antenna pattern of each detector at a given time. The best, worst and average efficiencies are also given.

	A1B2G1			A2B4G1			GAUSS1			GAUSS4			SG235Q15			SG820Q15		
	H1	L1	V1	H1	L1	V1	H1	L1	V1	H1	L1	V1	H1	L1	V1	H1	L1	V1
PF	42	42	49	49	48	47	66	62	50	28	29	57	35	38	31	42	42	63
KW	37	38	44	50	48	42	61	58	47	23	25	52	50	50	33	19	21	48
QT	46	45	48	59	56	46	72	68	50	40	43	52	71	67	53	48	47	65
PC	55	54	54	65	62	55	77	72	58	53	54	72	–	–	–	–	–	–
EGC	57	55	56	54	53	48	72	68	53	40	42	66	67	64	50	41	41	65
MF	40	40	51	53	52	51	64	61	50	27	29	63	38	41	23	10	11	33
ALF	43	43	52	57	55	52	68	63	53	36	39	68	42	43	25	16	19	44
Mean	46	45	51	55	53	49	69	65	52	35	37	61	43	43	31	25	26	45
Min	37	38	44	49	48	42	61	58	47	23	25	52	0	0	0	0	0	0
Max	57	55	56	65	62	55	77	72	58	53	54	72	71	67	53	48	47	65

conservatively assumed an error of 10 ms for all pipelines and for all signals. The event compatibility is tested using the estimated arrival times t_V, t_L and t_H of an event in each of the three detectors. For the two-fold coincidence analysis, the time difference in one of the three considered detector pairs must obey

$$|t_H - t_L| < \Delta_{HL}, \qquad \text{for a H1–L1 two-fold coincidence analysis,} \tag{5}$$

$$|t_H - t_V| < \Delta_{VHL}, \qquad \text{for a H1–V1 two-fold coincidence analysis,} \tag{6}$$

$$|t_L - t_V| < \Delta_{VHL}, \qquad \text{for a V1–L1 two-fold coincidence analysis,} \tag{7}$$

where $\Delta_{HL} = 20$ ms and $\Delta_{VHL} = 38$ ms are the time windows of coincidence for the H1–L1 pair and for the H1–V1 or L1–V1 detector pairs, respectively. For the three-fold coincidence analysis, conditions (5)–(7) must be fulfilled simultaneously.

4.2.2. FAR estimation. It has been verified that the FAR does not depend on the pipeline but only depends on the coincidence time window that is applied for the given network configuration following the formula given in section 4.1. This supports the hypothesis that the event triggers for all pipelines are distributed according to a Poisson distribution. The FAR has been estimated precisely for each pipeline using the trigger list obtained from noise; in order to cope with the expected low number of false alarm events per day, especially in the case of the three-fold coincidence (most of the pipelines end up with 0 or 1 false alarm event), we have increased artificially by 10 000 times the duration of the simulation. We do this by time shifting, by a step of 1 s, the event arrival time obtained from noise data streams. In practice, for a two-fold coincidence analysis, we consider the two trigger lists and add to the arrival time of all the events of one list an offset of 1 s. We perform the coincidence and determine the number of coincident events and then we repeat the operation but adding an offset of 2 s, etc. Note that the events of a N s time-shifted stream that are in the last N s are moved to the beginning of the time-shifted stream such that the duration of the two streams in coincidence is always identical to 24 h. A 1 s time shift is long enough (the typical event duration is much smaller than 1 s) to be sure of having different triggers list each time we add

Table 6. Detection efficiencies (in percent) obtained from the seven pipelines for a source located in the galactic center for a double coincidence search between a pair of interferometers. The efficiency has been estimated for each combination: Hanford–Livingston (HL), Hanford–Virgo (HV) and Livingston–Virgo (LV). The two-fold coincidence analysis has been done using events list obtained for a FAR of 0.1 Hz in each detector. The FAR of each two-fold coincidence involving Virgo is 7.5×10^{-4} Hz and 4×10^{-4} Hz for the Hanford–Livingston two-fold coincidence analysis (for all pipelines).

	A1B2G1			A2B4G1			GAUSS1			GAUSS4			SG235Q15			SG820Q15		
	HL	HV	LV	HL	HV	LV	HL	HV	LV	HL	HV	LV	HL	HV	LV	HL	HV	LV
PF	29	15	17	34	17	18	48	28	27	18	12	14	24	5	9	28	22	22
KW	25	10	13	34	15	17	43	22	24	13	9	10	35	9	14	11	4	6
QT	31	16	18	40	22	22	53	32	31	28	16	19	53	33	32	33	27	26
PC	38	25	25	50	32	30	59	42	38	38	35	36	–	–	–	–	–	–
EGC	40	27	27	38	21	21	54	35	33	28	21	24	50	29	29	28	22	22
MF	26	14	17	37	22	22	47	27	27	17	14	16	28	4	9	4	1	3
ALF	29	17	18	40	25	24	50	32	30	23	20	22	31	6	11	9	4	7
Mean	31	18	19	39	22	22	51	31	30	24	18	20	32	12	15	16	11	12
Min	25	10	13	34	15	17	43	22	24	13	9	10	0	0	0	0	0	0
Max	40	27	27	50	32	30	59	42	38	38	35	36	53	33	32	33	27	26

Table 7. Detection efficiencies (in percent) obtained from the seven pipelines for a source located in the galactic center for a three-fold coincidence search between the Hanford, Livingston and Virgo interferometers. The coincidence analysis has been done using events list obtained for a FAR of 0.1 Hz in each detector. The three-fold coincidence FAR is 3×10^{-6} Hz for all pipelines.

	A1B2G1	A2B4G1	GAUSS1	GAUSS4	SG235Q15	SG820Q15
PF	9	10	17	7	3	13
KW	6	9	13	4	6	2
QT	9	12	21	9	22	17
PC	14	19	30	23	–	–
EGC	16	12	23	13	19	13
MF	8	13	17	8	3	–
ALF	9	14	20	12	3	2
Mean	10	13	20	11	8	7
Min	6	9	13	4	0	0
Max	16	19	30	23	22	17

an additional 1 s offset. We checked that similar results are obtained with a longer time offset. For the three-fold analysis, a similar action is done on two of the three trigger lists; a 1 s offset is added to one of the trigger lists, and a 2 s offset is added to the other. That guarantees that at each step we perform coincidence analysis with trigger lists as if we had simulated new data streams.

For a two-fold coincidence search, the FAR is $(7.5 \pm 0.1) \times 10^{-4}$ Hz for a pair involving the Virgo (7.6×10^{-4} Hz expected), and $(4.03 \pm 0.03) \times 10^{-4}$ Hz for the Livingston–Hanford pair (4.1×10^{-4} Hz expected). For the three-fold coincidence, the FAR is $(3.07 \pm 0.03) \times 10^{-6}$ Hz (3.04×10^{-6} Hz expected).

4.2.3. Two-fold, three-fold and combined two-fold analysis. In tables 6 and 7, we give the detection efficiencies obtained for the two-fold coincidence and the three-fold coincidence analysis, respectively. It is interesting to note that for a given waveform the three-fold coincidence efficiencies of the pipelines differ significantly. The maximum (30%) and average

Table 8. Detection efficiencies (in percent) obtained by the seven pipelines for a source located in the galactic center for a double coincidence search between pairs of interferometers. The two-fold coincidence analysis has been done using event lists compiled such that the two-fold coincidence false alarm rate is 10^{-6} Hz. The efficiency has been estimated for each combination: Hanford–Livingston (HL), Hanford–Virgo (HV) and Livingston–Virgo (LV).

	A1B2G1			A2B4G1			GAUSS1			GAUSS4			SG235Q15			SG820Q15		
	HL	HV	LV	HL	HV	LV	HL	HV	LV	HL	HV	LV	HL	HV	LV	HL	HV	LV
PF	23	9	11	29	10	13	43	18	20	13	5	7	15	1	4	22	12	15
KW	19	5	9	27	7	11	38	12	16	9	3	5	29	4	9	7	2	4
QT	25	8	12	35	12	16	48	22	22	22	9	12	48	25	25	26	16	18
PC	33	15	18	39	20	20	53	32	30	30	23	24	–	–	–	–	–	–
EGC	35	18	20	31	11	14	47	24	24	20	13	15	43	19	21	21	10	14
MF	20	7	10	30	12	15	40	15	18	10	6	8	18	–	3	–	–	–
ALF	23	8	12	34	14	16	43	20	22	16	11	14	21	1	4	4	–	2
Mean	25	10	13	32	12	15	45	20	22	17	10	12	25	7	9	11	6	8
Min	19	5	9	27	7	11	38	12	16	9	3	5	0	0	0	0	0	0
Max	35	18	20	39	20	20	53	32	30	30	23	24	48	25	25	26	16	18

(20%) values obtained for GAUSS1 are low due to the non-optimum alignment of the three detectors. On the other hand, we end up with a FAR which is easily manageable, with less than one false alarm per day. This number is not achievable by any individual interferometer search. However, requiring coincidence among three interferometers that are not optimally aligned might not be the best strategy, compared to a two-fold coincidence search using Hanford and Livingston, which are well aligned. Note that, as expected, the efficiency of the Livingston–Hanford pair is always higher than any pair involving Virgo. Among the two other pairs, Virgo–Hanford is the worst due to the least optimal antenna response overlap. The results of the two-fold coincidence, given in table 6, indicate that on average the efficiency can be up to 70% higher than in the three-fold coincidence case, but the FAR remains high (a few 10^{-4} Hz). We thus estimate the efficiency of the two-fold coincidence analysis at the FAR of the three-fold coincidence analysis to be 10^{-6} Hz. The results are summarized in table 8. The two-fold efficiency is higher than the three-fold efficiency (comparison done at the same FAR) and, of course, the Hanford–Livingston pair is always favored compared to any pair including the Virgo detector. One can also require the detection of events in one of the three pairs of interferometers. The main advantage of this strategy is to reduce the FAR because of the coincidence constraint, while recovering events which are located in a sky zone for which only two detectors are sensitive. The results are summarized in table 9 for all pipelines. The combined two-fold coincidence analysis has been done using event lists obtained for a FAR of 10^{-6} in each pair of detectors, such that the combined two-fold analysis FAR is 3×10^{-6} Hz; it is the sum of the FAR of the two-fold coincidence from which the events that are actually common to the three pairs of interferometers must be subtracted two times. This number of events is given by the three-fold FAR which is at least three orders of magnitude lower than the two-fold FAR, and then can therefore be neglected; this can be directly compared to the three-fold coincidence FAR (which was used to make table 7) of 3×10^{-6} Hz.

4.3. Coincidence searches using the frequency information

Some of the burst pipelines (QT, PF, KW and EGC) are able to estimate the characteristics of the events in the frequency domain. Specifically, these are the frequency bandwidth (defined by $f_{\min}$ and $f_{\max}$) and the peak frequency (f_{peak}) which corresponds to the template

Table 9. Detection efficiencies (in percent) obtained by the seven pipelines for a source located in the galactic center requiring that at least one pair of interferometers among the three detects the signal. This combined two-fold coincidence analysis has been done using event lists obtained for a FAR of 10^{-6} Hz in each pair of detectors, such that the combined two-fold analysis FAR is 3×10^{-6} Hz identical to the three-fold analysis.

HL ∪ HV ∪ LV	A1B2G1	A2B4G1	GAUSS1	GAUSS4	SG235Q15	SG820Q15
PF	33	39	60	19	19	34
KW	26	36	52	14	38	11
QT	35	48	66	32	67	40
PC	56	67	76	55	–	–
EGC	52	43	66	32	60	32
MF	28	43	55	17	20	–
ALF	33	47	60	28	25	6
Mean	38	46	62	28	33	18
Min	26	36	52	14	0	0
Max	56	67	76	55	67	40

or wavelet coefficient that has the highest SNR. The peak frequency is thus not necessarily in the middle of the frequency bandwidth. Those coincidence searches whose results are given in section 4.2 considered only the timing information. The QT pipeline used in the LSC is actually performing a combined coincidence search requesting timing and frequency coincidence. It has been shown [33] that the QT coincidence search pipeline can reach a better efficiency (of a few percent) for the same FAR when using the frequency information. It is worth mentioning that the time and frequency coincidence performed in the LSC QT pipeline is done before the event extraction; this results in pruning overlapping templates. In this study, the time and frequency coincidence is done using event lists.

In this study, we tried to estimate the benefit of adding the frequency information to a coincidence search. For this, we used the trigger lists generated for each interferometer at 0.1 Hz, and applied the same timing coincidence plus a constraint on the overlap of the bandwidth of the triggers:

$$f^i_{\max} > f^j_{\min} \quad \text{if} \quad f^i_{\min} < f^j_{\min} \qquad \text{or} \qquad f^j_{\max} > f^i_{\min} \quad \text{if} \quad f^i_{\min} > f^j_{\min}, \tag{8}$$

where i and j are the indices of two of the three detectors. We estimated the efficiencies of the three pipelines on the test-case signals for the two-fold and three-fold coincidence searches and compared them to the results given in tables 6 and 7 (time-only coincidence). The efficiencies obtained were very similar (with a loss lower than 1%) to those obtained for the time-only coincidence search. The FAR is reduced, but in a rather moderate way depending on the pipelines: a factor of 0.67 for EGC and KW, a factor of 0.4 for PF and a factor of 0.2 for QT for the three-fold coincidence search. The FAR reduction factors are given in table 10 for the different network configurations.

In addition, we have also tried to use the peak frequency information instead of the bandwidth in order to determine if events are coincident in the frequency domain. The event frequency compatibility test is then

$$\left| f^i_{\text{peak}} - f^i_{\text{peak}} \right| < \Delta f, \tag{9}$$

where Δf has been varied such as the efficiency remains constant compared to a time-only coincidence analysis. The FAR reduction was found to be slightly higher compared to the bandwidth overlap coincidence constraint. This is especially the case for PF, for which the FAR of a three-fold coincidence is reduced by a factor 0.08 compared to the time-only coincidence, keeping for all test-case waveforms the same efficiency. But for the other

Table 10. FAR (in Hz) obtained by the four burst pipelines that estimate the frequency characteristics of the events in this study (QT, PF, KW and EGC). The results are given for a time-only coincidence search and for the time-and-frequency coincidence search. In the latter case, one requests that the frequency bandwidth of events overlaps.

Network	VH	VL	HL	VHL
FAR (time-only) QT PF KW and EGC	7.6×10^{-4}	7.6×10^{-4}	4.0×10^{-4}	3.0×10^{-6}
FAR (time and frequency) QT	3.2×10^{-4}	3.2×10^{-4}	1.7×10^{-4}	4.9×10^{-7}
Reduction factor QT	0.4	0.4	0.4	0.2
FAR (time and frequency) PF	5.0×10^{-4}	5.0×10^{-4}	2.6×10^{-4}	1.2×10^{-6}
Reduction factor PF	0.7	0.7	0.7	0.4
FAR (time and frequency) KW	6.2×10^{-4}	6.2×10^{-4}	3.4×10^{-4}	2.0×10^{-6}
Reduction factor KW	0.8	0.8	0.9	0.7
FAR (time and frequency) EGC	6.2×10^{-4}	6.2×10^{-4}	3.7×10^{-4}	2.2×10^{-6}
Reduction factor EGC	0.8	0.8	0.9	0.7

pipelines (QT, KW and EGC), the signal efficiency drops by at least 10% absolute for some of the waveforms (mainly the large bandwidth signals such as A1B2G1 or GAUSS1). Indeed, for large bandwidth signals, these pipelines fail to estimate precisely the peak frequency, which hence seems not to be a robust enough parameter to be used for a time-and-frequency coincidence pipeline (to maintain the efficiency to the time-only coincidence value, it was mandatory to increase Δf such that no FAR reduction was observed); an exception to this is the PF pipeline.

4.4. Comparisons and detection strategy discussion

In the previous sections, we have estimated the efficiency of seven pipelines for different search strategies: three-fold, two-fold and combined two-fold coincidence. We have first shown that the performance of some of the pipelines depends strongly on the waveform. The extreme case is reached by the correlator PC which performs very well for the DFM and Gaussian waveforms, but fails at detecting the sine-Gaussian waveforms. On the other hand, the EGC and QT pipelines' performance remains very high for all kinds of waveforms. The PF and KW pipelines have similar performance whatever the waveform, but perform on average a bit less efficiently.

The two-fold coincidence results show that one can decrease the FAR from 0.1 Hz (8640 events per day) to a few 10^{-4} Hz (30 events per day), while maintaining a detection efficiency at an acceptable level. The best performances are, of course, obtained from the Hanford–Livingston pair; these efficiencies are, on average for all pipelines, 0.15 lower than the individual interferometer pipeline efficiencies working at a 0.1 Hz FAR. The efficiency of the HV or LV combination is approximately two-thirds of the HL efficiency, due to the different alignment of LIGO and Virgo. To reduce the FAR significantly, one has to request a three-fold coincidence; we then end up with two false alarm events per week. However, due to the non-optimum alignment of the three interferometers, the detection efficiency drops to 10–20% on average for the test-case waveforms. To overcome the problem of the non-optimum alignment of the three interferometers, while keeping a very low number of false alarm events, the best strategy seems to be such as to request the detection of an event in at least one of the three pairs of detectors (combined two-fold coincidence). We have seen that, for the same FAR (two events per week), the efficiency is three times higher, on average, compared to a three-fold coincidence search. The best performing pipeline efficiency is then between 40% and 76%, depending on the waveform for two false alarm events per week.

Moreover, comparing the two-fold coincident search obtained with the Hanford–Livingston pair to the combined two-fold coincidence, we have shown that, on average for all waveforms, the detection efficiency is increased by 50% by adding Virgo to the Hanford–Livingston network (we have checked that the two-fold coincidence Hanford–Livingston efficiencies for a FAR of 3×10^{-6} Hz are very similar to those given in table 8 for a FAR of 10^{-6} Hz. The difference is at maximum as high as 0.02). If we consider the results of the two-fold combined search in table 9, QT and EGC are the two best performing pipelines over the six test-case waveforms. The others have the main drawback of performance depending on the waveforms.

In addition, the figure of merit of the time-only coincident search can be improved if one requires that coincident events have similar frequency characteristics. We have seen that the reduction of the false alarm events actually depends, from one pipeline to another, on the frequency estimation of the event bandwidth. One can expect to reduce the false alarm event number by up to a factor 0.08 without losing any efficiency in the most favorable case (PF pipeline).

5. Combination of filters

In section 3, the detection potential of several pipelines has been compared using a few test-case waveforms. We have seen that a pipeline's performance is different from one waveform to another, and there is the indication that the pipelines are complementary and can cover the full range of tested waveforms. Conversely, for a given signal, it could be interesting to determine if all pipelines detect the same events. We would expect a gain of the detection efficiency by combining different filters' output. Of course, merging (OR analysis) the trigger lists of different pipelines increases the FAR. If the pipelines all detect the same events, it would then be more interesting to request that the filters' combination keep only the events seen by all the considered filters (AND analysis). But in that case, the detection probability will always be dominated by the filter that is least sensitive. We could however expect that the pipelines are not sensitive to the same noise events and hence see a reduction of the FAR. In this study, we have considered the 120 possible combinations given 7 pipelines, from 2 filters up to the 7 filter combination. To fairly compare the results, we need to derive the ROC curves and compare them to the single pipeline curves.

We started by using the seven pipelines' trigger lists provided for the eight test-case waveforms injected into the V1 and H1 data sets (optimal orientation) with a SNR of 5 and 10, and for 3 FAR (0.1 Hz, 0.01 Hz and 0.005 Hz). We chose identical FAR for all filters for the sake of simplicity, while they might not correspond to the optimal choice. Next, from the single method trigger lists we produced a new set of triggers; a single gravitational wave burst candidate was created via the merger of triggers that were overlapping or temporally closer than 0.1 s. This condition was introduced in order to account for the maximum timing error of the filters without merging triggers due to noise with real signal ones (we start from triggers lists computed at a maximum FAR of 0.1 Hz). The non-merged triggers are simply added to the new list for the OR analysis. These prescriptions allowed us to compute both the FAR for the combination of triggers as well as the efficiency. Then, for each type of combination (two filters, three filters, etc) we keep the one having the best ROCs. In such a way we can, at the end, compare the six combined ROCs with the seven pipelines' ROC.

The main conclusion of this analysis is that no combination shows a ROC consistently better than the best single method ROC, for all waveforms. As expected, the AND analysis helps at reducing the FAR, but the efficiency decrease is too large to provide any real gain. The result is robust with respect to the injection signal SNR and the choice of interferometer.

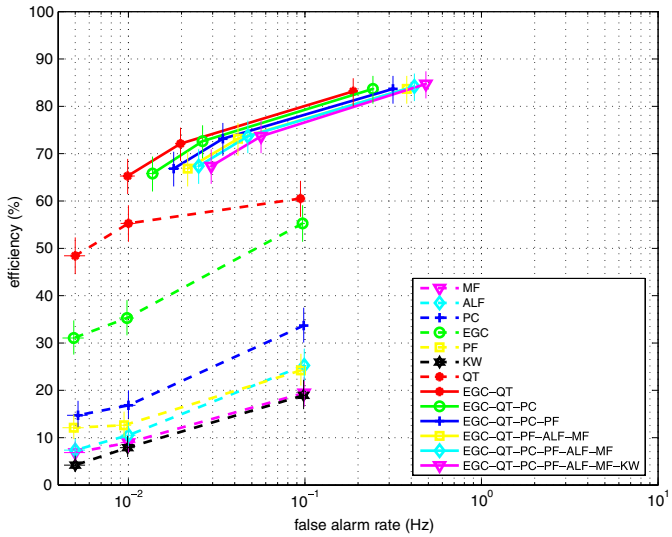

Figure 11. Three operating points for single methods and the best performing combination of methods in the V1 data for an injected sine-Gaussian SG235Q5 with a SNR of 5. The OR analysis obtained its best performance on this sine-Gaussian test-case waveform. The vertical error bars have been computed with a binomial fit and the horizontal ones by Poisson statistics. It can be noted that adding new methods to the EGC–QT combination only translates the ROC horizontally. This means that in this case adding methods increases the number of false alarms but not the number of observed injections.

Occasionally, for a specific waveform, like the sine-Gaussian SG235Q5 (as shown in figure 11), the OR combination of the two best pipelines mildly improves the ROC; the relative efficiency gain is between 10% and 30% depending on the FAR. But, this improvement depends on the waveform; for the A1B2G1 and GAUSS4 signals the performance is as good as the best pipeline, or even worse. In figure 11, we can also note that actually QT performs best on sine-Gaussian SG235Q5, and combining QT with EGC increases the detection efficiency from 55% (QT only) to 65% (QT or EGC) at a FAR of 10^{-2} Hz. Since these results do not encourage the combination of methods, we decided not to pursue it for the network study where only combinations of interferometers' configurations have been thoroughly studied.

6. Source sky location reconstruction

6.1. Introduction

In addition to the increase of the detection probability of a burst gravitational wave, the other significant advantage of the LIGO and Virgo detector network is to provide the possibility to estimate the position of the source on the sky. It is well known [39] that a minimum of three detectors is mandatory in order to determine the source sky position, even if an ambiguity remains between two positions symmetric with respect to the plane defined by the three detectors. So, the LIGO–Virgo network is the first step toward gravitational wave astronomy that includes source localization. The source coordinates on the sky are right ascension (α) and declination (δ). A method [25] has been developed for estimating the source position using only the arrival time t_i of the gravitational wave in each detector, and its associated arrival time error σ_i. This method has the advantage of being fast and independent of the pipeline.

Three-fold coincidence search events found by the seven pipelines in the 24 h of data with a FAR of 3×10^{-6} Hz have been considered in this sky location study. A comparison of the source reconstruction accuracy of each pipeline is presented below.

6.2. Method

Each burst pipeline provides a list of three-fold coincidence events defined by the arrival time and the event SNR reconstructed in the three detectors. We then have to estimate the arrival time error for each event. In this study, for the sake of simplicity, we have taken the following relation that is exact for a Gaussian signal of half-width 1 ms detected by PC [38]:

$$\sigma_i = \frac{1.4}{\mathrm{SNR}_i}\mathrm{ms}. \tag{10}$$

It should be noted that, in general, the burst pipelines can determine, event-by-event, the error of the arrival time, for instance, by taking into account the results given in section 3.5. We have checked that the results weakly depend on the error parametrization given in (10) as the result is primarily constrained by the arrival time values. To estimate α and δ a least-square minimization has been used. Our χ^2 function is defined by

$$\chi^2 = \sum_{i=1}^{n} \frac{\left(t_i - \left(t_0 + \Delta_i^{\mathrm{Earth}}(\alpha, \delta)\right)\right)^2}{\sigma_i^2}, \tag{11}$$

where t_0 is the arrival time of the gravitational wave at the center of the Earth and $\Delta_i^{\mathrm{Earth}}(\alpha, \delta)$ is the delay between the center of the Earth and the ith detector at a given sidereal time (and only depends on α and δ). First of all, this definition of the χ^2 function allows the fitting of uncorrelated data, while the usual reconstruction using two time differences between detector implies variables with correlated errors deserving a more difficult treatment. By introducing t_0, there is no reference detector D_1 used to compute timing differences. The second advantage is that the network is not limited to three detectors, and the addition of other detectors is straightforward. Nevertheless, this method requires that the event be seen by all the detectors above a given threshold, whereas coherent methods do not need this first selection step.

6.3. Results

Figure 12 shows an example of the reconstructed source coordinate distributions using the 24 h of simulated data. It has been obtained using 456 GAUSS1 events detected by the PC pipeline. These distributions include the effect of modulation due to the Earth's rotation over 24 h, which then induces some variation of the event arrival time errors. The errors on α and δ are about 1° (respectively, 0.7° and 1°). Table 11 gives a summary of angular reconstruction obtained for each pipeline on all waveforms studied. As expected, the estimation accuracy is mainly dependent on the arrival time measurement accuracy. In this case the correlator pipelines (PC and EGC) and QT produce the best results. The achieved precision depends also on the considered waveform. The best accuracy is obtained for waveforms which have rather simple shape, such as clearly defined peak (like DFM A1B2G1 or GAUSS1). In contrast, when the waveforms become more complex (DFM A2B4G1, sine-Gaussian), all the pipelines that make very few assumptions on the exact waveform (MF, ALF, PF, KW) fail at precisely locating the source. QT and EGC perform, as expected, the best for sine-Gaussian signals. One should also note that pipelines having a large timing bias have a poor source reconstruction estimation, due to the fact that the bias is mainly different in each detector. We have seen that bias is predominantly due to the use of nonzero phase whitening filtering. Since LIGO

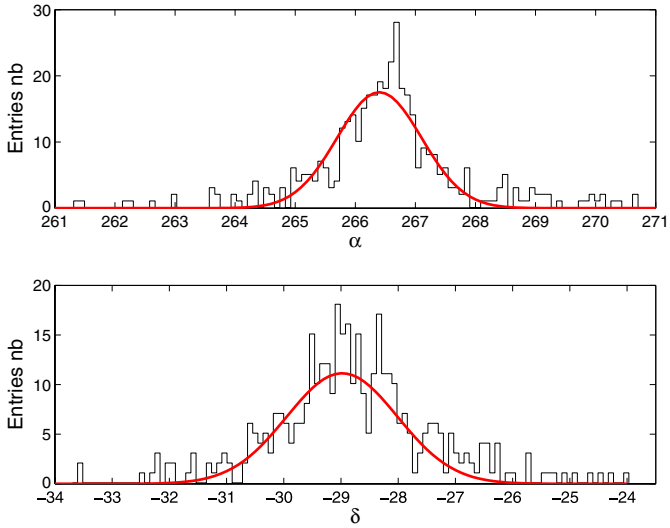

Figure 12. Distribution of source coordinates α and δ (in degrees) obtained for a GAUSS1 waveform detected with the PC pipeline in the LIGO–Virgo network. The source has been placed in the direction of the galactic center and emits signals regularly over 24 h. The curve is the result of a Gaussian fit of the data.

and Virgo have different power spectrum shapes the bias is different. That tends to prove that the source position determination should be somehow decoupled from the detection problem. Once good candidates are detected, techniques including more information (for instance rough waveform estimation as needed by Markov Chain Monte Carlo algorithms [23]) should be used to estimate the source position.

7. Summary

In this study, we have compared different pipelines developed both in the LSC and Virgo for the search for unmodeled gravitational wave bursts. For both Virgo and LIGO data sets, we have evaluated the pipeline's performance and validated their ability to detect a signal. Among all the seven pipelines studied, we have especially shown that some are more efficient than others. We have demonstrated the benefits of a LIGO–Virgo combined search for the detection of a signal; adding Virgo to the Hanford–Livingston interferometer network can increase the detection efficiency by 50% (without increasing the false alarm rate). We have shown that the combined two-fold coincident search is three times more efficient than a three-fold coincident search (for the same expected number of false alarm events). In contrast, combining the filters' trigger lists obtained on the same data stream does not improve the detection potential of the burst analysis. The second advantage of the LIGO–Virgo network is its capability to locate a source. We have shown that in the most favorable case we can expect to reconstruct the source position with a precision of the order of 1° for both the right ascension and the declination. The position determination performance is not as good when the waveform is complex in structure. It would be interesting, in the near future, to compare the performance obtained by the combined two-fold coincident search to coherent searches [40] using the same network of interferometers, as well as their respective performance to reconstruct the source position [17].

Table 11. Reconstructed source coordinates obtained by the burst pipelines using the method described in section 6.2 for the different waveforms studied. Standard deviation are also given. The galactic center is located at (266.4°, −28.98°). The number of three-fold coincident events used to determine the sky position is also given.

		A1B2G1	A2B4G1	GAUSS1	GAUSS4	SG235Q15	SG820Q15
	α	265.0 ± 4.0	260.3 ± 1.9	263.0 ± 7.0	250.0 ± 14.0	258.0 ± 29.0	266.0 ± 5.0
PF	δ	−28.0 ± 7.0	−27.0 ± 8.0	−29.0 ± 13.0	−13.0 ± 21.0	−15.0 ± 33.0	−28.0 ± 10.0
	#	126	138	255	104	37	184
	α	265.0 ± 5.0	264.7 ± 9.0	265.0 ± 8.0	265.0 ± 22.0	264.0 ± 29.0	266.0 ± 6.0
KW	δ	−26.5 ± 9.0	−26.0 ± 13.0	−25.0 ± 12.0	−29.0 ± 23.0	−15.0 ± 32.0	−27.0 ± 10.0
	#	93	159	227	61	102	38
	α	266.0 ± 1.5	264.0 ± 6.0	266.0 ± 4.0	268.0 ± 13.0	266.0 ± 11.0	267.0 ± 3.0
QT	δ	−28.8 ± 4.6	−28.0 ± 12.0	−28.5 ± 8.0	−25.0 ± 17.0	−25.0 ± 16.0	−29.0 ± 6.0
	#	134	179	300	131	318	238
	α	266.5 ± 0.5	266.7 ± 1.3	266.4 ± 0.7	266.6 ± 2.0		
PC	δ	−29.0 ± 0.6	−29.1 ± 2.3	−29.0 ± 1.0	−29.1 ± 3.6	–	–
	#	240	273	456	334		
	α	266.3 ± 0.3	265.6 ± 3.0	266.2 ± 1.0	266.7 ± 3.0	265.0 ± 9.0	267.1 ± 3.0
EGC	δ	−28.9 ± 0.4	−29.2 ± 7.0	−29.0 ± 1.7	−28.1 ± 6.0	−28.7 ± 13.0	−29.0 ± 4.5
	#	223	172	338	193 ?	269	191
	α	266.5 ± 0.5	261.3 ± 1.3	263.7 ± 8.0	258.5 ± 18.0	263.0 ± 30.0	
MF	δ	−29.0 ± 0.6	−27.3 ± 4.0	−30.2 ± 14.0	−10.0 ± 22.0	−24.0 ± 29.0	–
	#	112	182	243	115	41	
	α	265.5 ± 1.8	258.0 ± 14.0	260.1 ± 1.7	258.0 ± 3.0	260.0 ± 23.0	264.0 ± 10.0
ALF	δ	−27.0 ± 5.0	−25.9 ± 20.0	−29.4 ± 7.0	−17.0 ± 10.0	−27.0 ± 28.0	−28.0 ± 10.0
	#	132	208	288	175	50	32

The next step of this work is to analyze test sets of real data from LIGO and Virgo. This will bring forward other issues to be studied, such as the examination and handling of the quality of the data in a combined search. One of the key issues will be the non-stationarity of the data sets (the increase of the noise during short periods, for instance due to seismic activity) that can produce higher FAR than what has been optimally considered in this study. That could have an impact especially on the combined two-fold coincidence analysis FAR. Another aspect of the GW burst search is the glitches present in the real interferometer data. If a careful analysis is undertaken in order to understand the origin of the glitches, and thereby allowing one to suppress most of them, then dedicated techniques to distinguish real GW burst signal from noise transients could be used [41].

Acknowledgments

LIGO Laboratory and the LIGO Scientific Collaboration gratefully acknowledge the support of the United States National Science Foundation for the construction and operation of the LIGO Laboratory and for the support of this research. NC also acknowledges the support of the Fulbright Scholar Program. Virgo is supported by the CNRS (France) and INFN (Italy). Support was also provided by the MIT-France alliance award.

Appendix. Parameters used for the robustness test

Table A1 provides the parameters associated with the waveforms used in this study. These are the signals that were used to test the coverage of the GW parameter space by the burst search pipelines in section 3.4.

Table A1. Parameters of the 100 waveforms used to test the robustness of the different burst pipelines: 50 waveforms are simulated core collapse, while the 50 other (WN) are filtered white noise bursts. DFM waveforms (Newtonian or relativistic simulation) are taken from [4], BO waveforms (Newtonian) are taken from [5] and ZM (Newtonian) waveforms are extracted from [3]. The peak frequency, bandwidth and duration of the signals have been computed as explained in section 2.2.1.

Name	Peak frequency (Hz)	Bandwidth (Hz)	Duration (s)
DFM (New.) A1B2G1	365.3	182.1	0.0012
DFM (New.) A4B1G1	429.5	324.4	0.0012
DFM (New.) A4B5G5	138.1	84.9	0.0030
DFM (Rel.) A3B1G1	552.5	585.5	0.0007
DFM (Rel.) A3B2G1	433.3	428.9	0.0018
DFM (Rel.) A3B2G2	622.3	621.1	0.0006
DFM (Rel.) A3B4G2	77.9	52.3	0.0063
DFM (Rel.) A4B4G5	67.3	63.1	0.0110
DFM (Rel.) A1B3G2	670.1	518.4	0.0006
DFM (Rel.) A4B5G4	69.7	63.2	0.0079
DFM (Rel.) A4B1G1	288.8	281.2	0.0047
DFM (Rel.) A4B1G2	349.8	341.8	0.0036
DFM (Rel.) A3B3G2	83.7	78.7	0.0135
DFM (Rel.) A4B2G2	201.1	194.3	0.0082
BO s11A1000B0.3	197.0	109.9	0.0023
BO s11A50000B0.6	59.0	31.6	0.0067
BO s11A500B0.4	92.2	56.6	0.0089
BO s11A1000B0.4	81.6	44.7	0.0048
BO s15A500B0.4	74.8	73.0	0.0085
BO s15A1000B0.3	239.8	157.7	0.0017
BO s15A1000B0.6	51.3	34.6	0.0079
BO s15nonrot	133.4	132.7	0.0221
BO s20A50000B0.1	417.1	138.2	0.0011
BO s20A500B0.2	202.2	171.4	0.0031
BO s20A50000B0.2	401.7	171.5	0.0011
BO s20A50000B0.5	267.0	216.2	0.0015
BO s20nonrot	217.0	181.9	0.0093
BO s20A1000B0.4	83.0	50.9	0.0285
BO s25A500B0.2	198.0	173.3	0.0310
BO s20A1000B0.5	63.3	40.4	0.0363
BO s20A500B0.1	394.1	271.2	0.0010
ZM (New.) A1B1G3	550.3	311.4	0.0007
ZM (New.) A2B5G4	74.0	70.0	0.0067
ZM (New.) A4B2G5	395.2	386.6	0.0011
ZM (New.) A2B5G5	55.2	42.3	0.0031
ZM (New.) A3B4G3	112.4	59.7	0.0038
ZM (New.) A3B4G4	147.3	137.0	0.0044
ZM (New.) A2B2G3	588.3	165.7	0.0009
ZM (New.) A3B4G5	102.9	77.3	0.0032
ZM (New.) A3B2G1	193.0	156.0	0.0218
ZM (New.) A4B1G1	399.3	303.1	0.0132
ZM (New.) A1B3G1	110.1	104.3	0.0272
ZM (New.) A2B3G2	218.0	143.0	0.0026
ZM (New.) A3B2G2	370.3	230.8	0.0012
ZM (New.) A3B2G4	678.6	275.2	0.0007
ZM (New.) A4B1G4	535.0	191.4	0.0013
ZM (New.) A3B2G5	318.7	297.9	0.0022
ZM (New.) A4B1G5	473.3	483.3	0.0018

Table A1. (Continued.)

Name	Peak frequency (Hz)	Bandwidth (Hz)	Duration (s)
ZM (New.) A3B3G2	163.9	106.9	0.0034
ZM (New.) A4B2G2	248.9	171.6	0.0023
WN	155.3	171.6	0.0023
WN	200.6	176.0	0.0312
WN	101.1	21.7	0.0059
WN	97.2	10.4	0.0125
WN	100.6	8.1	0.0175
WN	97.0	10.8	0.0272
WN	110.1	43.8	0.0023
WN	121.6	78.8	0.0170
WN	118.3	99.5	0.0027
WN	206.1	193.9	0.0024
WN	250.2	43.1	0.0028
WN	248.3	7.6	0.0186
WN	247.2	55.7	0.0044
WN	398.0	39.6	0.0236
WN	413.6	200.8	0.0189
WN	437.0	400.9	0.0120
WN	495.2	320.6	0.0157
WN	503.6	11.0	0.0137
WN	503.0	9.0	0.0170
WN	519.3	41.6	0.0035
WN	535.7	118.9	0.0059
WN	766.4	541.2	0.0031
WN	696.4	553.8	0.0110
WN	699.7	7.6	0.0193
WN	695.2	85.4	0.0026
WN	693.8	16.2	0.0204
WN	742.3	443.6	0.0016
WN	943.4	16.2	0.0110
WN	976.4	178.8	0.0026
WN	912.7	203.9	0.0144
WN	1020.0	375.3	0.0037
WN	1049.1	31.9	0.0393
WN	1068.9	455.2	0.0338
WN	1062.5	577.2	0.0330
WN	1299.8	8.5	0.0181
WN	1300.0	32.8	0.0237
WN	1316.1	105.3	0.0020
WN	1276.6	353.4	0.0247
WN	1498.0	25.1	0.0051
WN	1586.1	439.9	0.0057
WN	1559.6	354.4	0.0025
WN	1494.2	716.4	0.0303
WN	1704.2	22.0	0.0054
WN	1703.7	34.2	0.0150
WN	1723.2	309.8	0.0141
WN	1718.8	455.2	0.0173
WN	1704.4	649.7	0.0165
WN	1704.4	642.5	0.0320
WN	1699.2	45.9	0.0244
WN	1991.7	164.3	0.0180

References

[1] Abbott B *et al* (the LIGO Scientific Collaboration) 2006 *Class. Quantum Grav.* **23** S51–6
[2] Acernese F *et al* (the Virgo Collaboration) 2006 *Class. Quantum Grav.* **23** S63–9
[3] Zwerger T and Mueller E 1997 *Astron. Astrophys.* **320** 209
[4] Dimmelmeier H, Font J A and Mueller E 2002 *Astron. Astrophys.* **393** 523
[5] Ott C *et al* 2004 *Astrophys. J.* **600** 834
[6] Shibata M and Sekiguchi Y I 2004 *Phys. Rev.* D **69** 084024
[7] Flanagan E E and Hughes S A 1998 *Phys. Rev.* D **57** 4535
[8] Baker J *et al* 2006 *Phys. Rev.* D **73** 104002
[9] Pretorius F 2005 *Phys. Rev. Lett.* **95** 121101
[10] Campanelli M *et al* 2006 *Phys. Rev. Lett.* **96** 111101
[11] Kokkotas K D and Schmidt B G 1999 Living Rev. Rel. http://www.livingreviews.org/lrr-1999-2
[12] Meszaros P 2006 *Rep. Prog. Phys.* **69** 2259–322
[13] Ferrari V, Miniutti G and Pons J A 2003 *Class. Quantum Grav.* **20** S841
[14] Damour T and Vilenkin A 2005 *Phys. Rev.* D **71** 063510
[15] Arnaud N *et al* 1999 *Phys. Rev.* D **59** 082002
[16] Ott C *et al* 2006 *Phys. Rev. Lett.* **96** 201102
[17] Gursel Y and Tinto M 1989 *Phys. Rev.* D **40** 3884
[18] Arnaud N *et al* 2003 *Phys. Rev.* D **68** 102001
[19] Astone P *et al* 2003 *Phys. Rev.* D **68** 022001
[20] Abbott B *et al* (the LIGO Scientific Collaboration) 2005 *Phys. Rev.* D **72** 062001
[21] Abbott B *et al* (the LIGO Scientific Collaboration and the TAMA Collaboration) 2005 *Phys. Rev.* D **72** 122004
[22] Poggi S *et al* 2006 *J. Phys. Conf. Ser.* **32** 198–205
[23] Beauville F *et al* 2008 Detailed comparison of LIGO and Virgo inspiral pipelines in preparation for a joint search *Class. Quantum Grav.* **25** 045001
[24] Beauville F *et al* 2005 *Class. Quantum Grav.* **22** S1293
[25] Cavalier F *et al* 2006 *Phys. Rev.* D **74** 082004
[26] The LSC programs are in the LSC Algorithm Library Applications software package LALAPPS http://www.lsc-group.phys.uwm.edu/daswg/projects/lalapps.html
[27] Caron B *et al* 1999 *Astropart. Phys.* **10** 369
[28] Buskilic D *et al* 2000 *Int. J. Mod. Phys.* D **9** 263–7
[29] Sutton P J 2007 Characterising the space of gravitational-wave bursts *LIGO Document* LIGO-PO70139-00-Z
[30] Flandrin P 1993 *Temps-Fréquence* (Paris: Ed. Hermes)
[31] Cuoco E *et al* 2001 *Class. Quantum Grav.* **18** 1727–51
[32] Guidi G *et al* 2004 *Class. Quantum Grav.* **21** S815–20
[33] Chatterji S *et al* 2004 *Class. Quantum Grav.* **21** S1809–18
[34] Pradier T *et al* 2001 *Phys. Rev.* D **63** 042002
[35] Welch P D 1967 *IEEE Trans. Audio Electroacoust.* **15** 70
[36] Arnaud N *et al* 2003 *Phys. Rev.* D **67** 102003
[37] Clapson A-C *et al* 2008 *Class. Quantum Grav.* **25** 035002
[38] Arnaud N *et al* 2003 *Phys. Rev.* D **67** 062004
[39] Boulanger J L *et al* 1989 *Astron. Astrophys.* **217** 381
[40] Klimenko S *et al* 2005 *Phys. Rev.* D **72** 122002
[41] Chatterji S *et al* 2006 *Phys. Rev.* D **74** 082005